Supporting Information

Pd nanoparticles decorated borophene nanosheets for intrinsic-polarization induced visible light photocatalysis

Bitan Pratihar,[‡a] *Animesh Jana,*[‡a,b] *Souvik Biswas,*[c] *and Sirshendu De*[*a]

[a] Department of Chemical Engineering, Indian Institute of Technology Kharagpur, Kharagpur 721302, India.

[b] CSIR-National Metallurgical Laboratory, Jamshedpur 83100, India.

[c]School of Medical Science and Technology Indian Institute of Technology Kharagpur, Kharagpur 721302, India.

[‡]These authors contributed equally

[*]Corresponding author E-mail: sde@che.iitkgp.ac.in

.

S1. Experimental Section

S1.1. Materials

Boron (≥95% (boron), MW: 10.81), Ciprofloxacin ($C_{17}H_{18}FN_3O_3$, ≥98%, MW: 331.34), Ibuprofen ($C_{13}H_{18}O_2$, ≥98%, MW: 206.28), Acetone (CH_3COCH_3, ≥99.5%, MW: 58.08), 2-Propanol ($(CH_3)_2CHOH$, ≥99.5%, MW: 60.10), Potassium bromide (KBr, ≥99.0%, MW: 119.00), Nafion (5 wt. % in lower aliphatic alcohols and water, contains 15-20% water), Sodium Sulphate (Na_2SO_4, ≥99.0%, MW: 142.04), *tert*-butyl alcohol ($(CH_3)_3COH$, ≥99.5%, MW: 74.12), *p*-Benzoquinone ($C_6H_4(=O)_2$, ≥98%, MW: 108.09), Potassium bromate, ≥99.8%, MW: 167.00), Acetonitrile (CH_3CN, ≥99.9%, MW: 41.05), Formic acid (HCOOH, ≥96%, MW: 46.03), Acetic acid (CH_3CO_2H, ≥99.7%, MW: 60.05), Sodium phosphate dibasic heptahydrate ($Na_2HPO_4.7H_2O$, 98.0-102.0%, MW: 268.07), Sodium chloride (NaCl, ≥99.0%, MW: 58.44), Iron (II) sulphate heptahydrate ($FeSO_4.7H_2O$, ≥99.0%, MW: 278.01), Potassium dihydrogen phosphate (KH_2PO_4, MW: 136.09), Magnesium nitrate hexahydrate ($Mg(NO_3)_2.6H_2O$, 99%, MW: 256.41), Indium tin oxide (ITO) were purchased from M/s, Sigma Aldrich, USA. Ethylene diamine tetra acetic acid disodium salt (EDTA-2Na, MW: 372.24) was procured from M/s. Merck Life Sciences Pvt. Ltd. Palladium chloride ($PdCl_2$, MW: 177.31), hydrazine hydrate (N_2H_5OH, 80%, MW: 50.06) and congo red ($C_{32}H_{22}N_6Na_2O_6S_2$, MW: 696.65) were obtained from M/s, Loba Chemie, Mumbai, India. Sodium hydroxide (NaOH, MW: 40) and nitric acid (HNO_3, 65%, MW: 63.01) were purchased from M/s, Merck (India) Ltd., Mumbai. Methanol (CH_3OH, MW: 32.04) was obtained from M/s. Spectrochem Pvt. Ltd., Mumbai, India. Ethanol (CH_3CH_2OH, 99.9%, MW: 46.07) was received from Jiangyin Darlly International Trade Co. Ltd., China.

Deionized (DI) water was used as a solvent for the preparation of all the solutions and was prepared from Millipore water purification system supplied by Merck (India) Pvt. Ltd. All the chemicals were of analytical grade and used as received without any further purification.

S1.2. Electrochemical measurements

Indium tin oxide (ITO) (1×1 cm^2) was sequentially cleaned in acetone, water, and ethanol for 30 min each using an ultrasonic cleaner and dried in a hot air oven at 60 ^oC. A slurry of Pd-B catalyst (1 mL) was prepared (Nafion: 90 μL, ethanol: 540 μL and deionized water: 370 μL), ultrasonicated for 3 hrs, deposited on ITO, and dried in a hot air oven at 60 ^oC. Electrochemical

studies were performed using Autolab (model: PGSTAT 302N, Metrohm Autolab B.V., Netherlands) in presence of visible light (24 W). All electrochemical measurements were performed in 0.1 M Na_2SO_4 + 0.04 M KOH solution in standard three-electrode setup, with Ag/AgCl electrode as reference, platinum (Pt) as counter electrode, and Pd-B catalyst slurry coated on ITO as working electrode. To obtain the Nyquist diagram from Electrochemical Impedance Spectra EIS, the AC frequency with RMS amplitude of 10 mV was varied from 10 kHz to 1 Hz with a set potential of 0.6 V (Ag/AgCl). The EIS plot and corresponding Bode phase plot were analyzed using NOVA 1.0.1. Transient photocurrent measurements of the photocatalysts were performed using Potentiostat/ Galvanostat/ EIS workstation (model: ZIVE SP1, Korea) under a 150 W Xe lamp.

S2. Results and Discussion

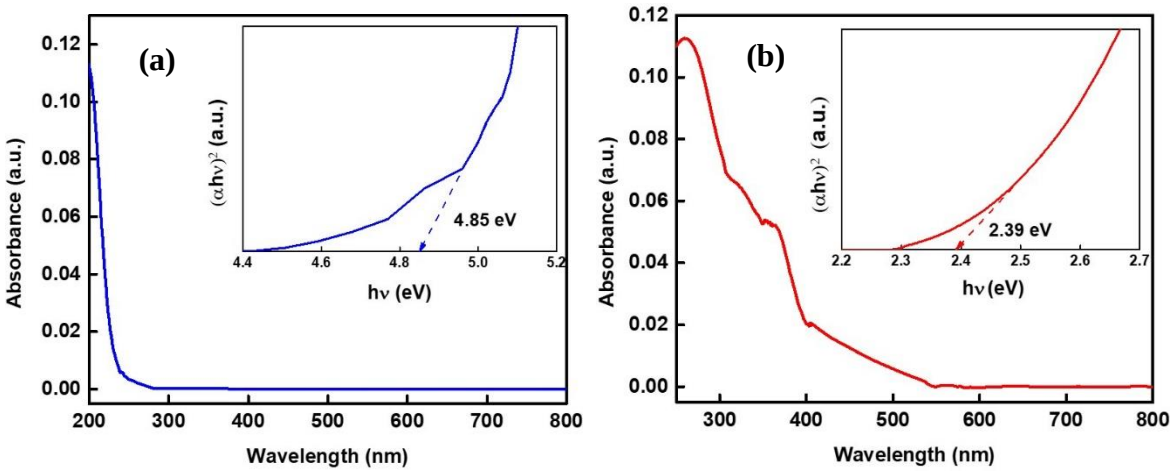

Fig. S1. UV-vis diffuse reflectance spectra of (a) borophene and (b) Pd-B.

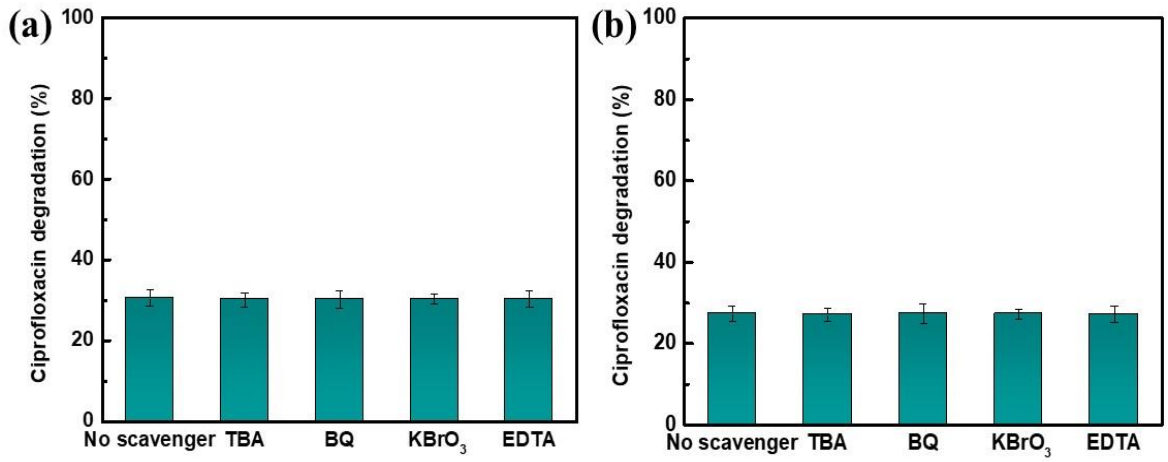

Fig. S2. CIP degradation efficiency of (a) borophene and (b) Pd nanoparticles in the presence of various quenching agents.

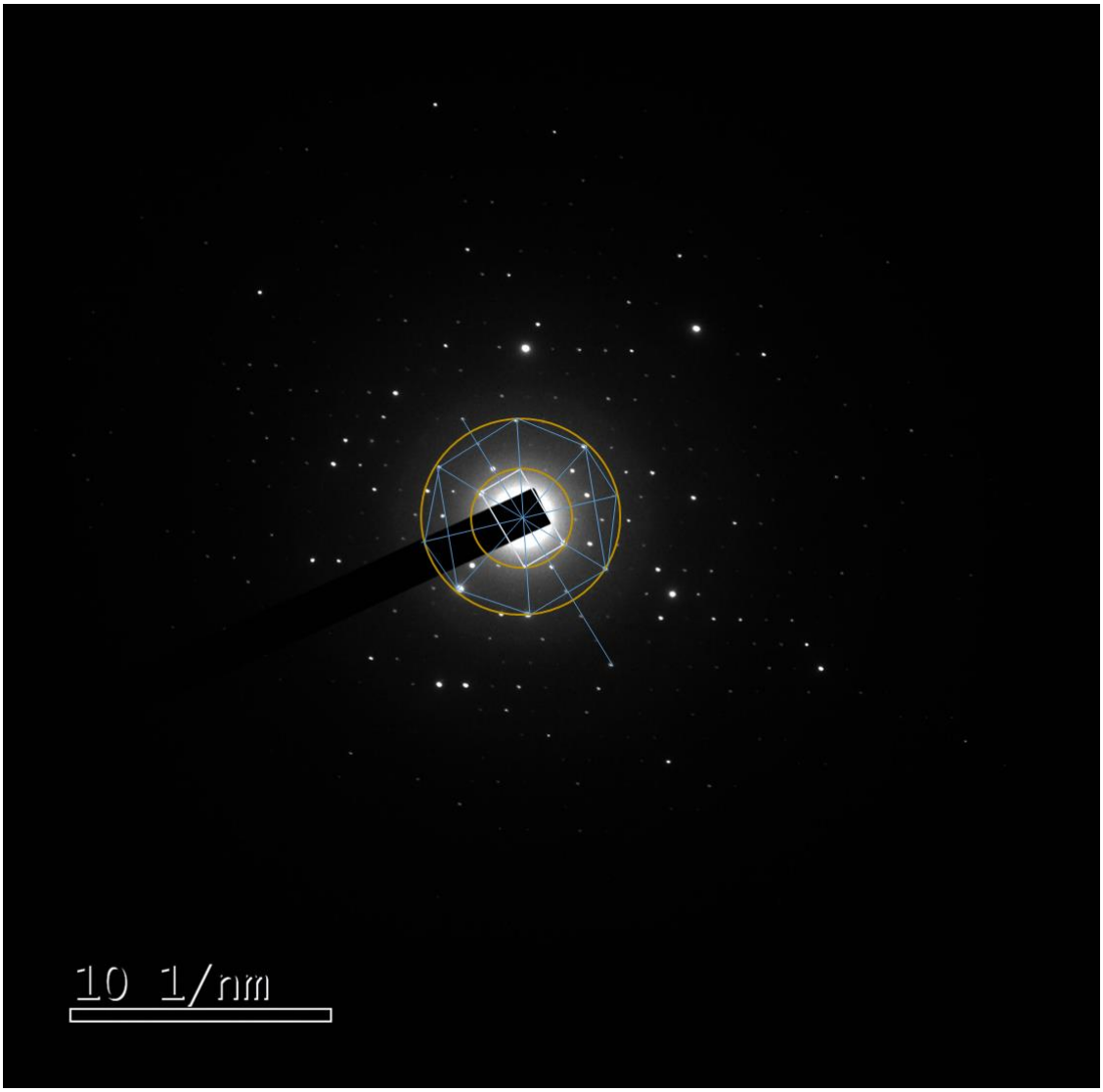

Fig. S3. SAED patterns showing six-fold and two-fold symmetry of freestanding borophene in acetone.

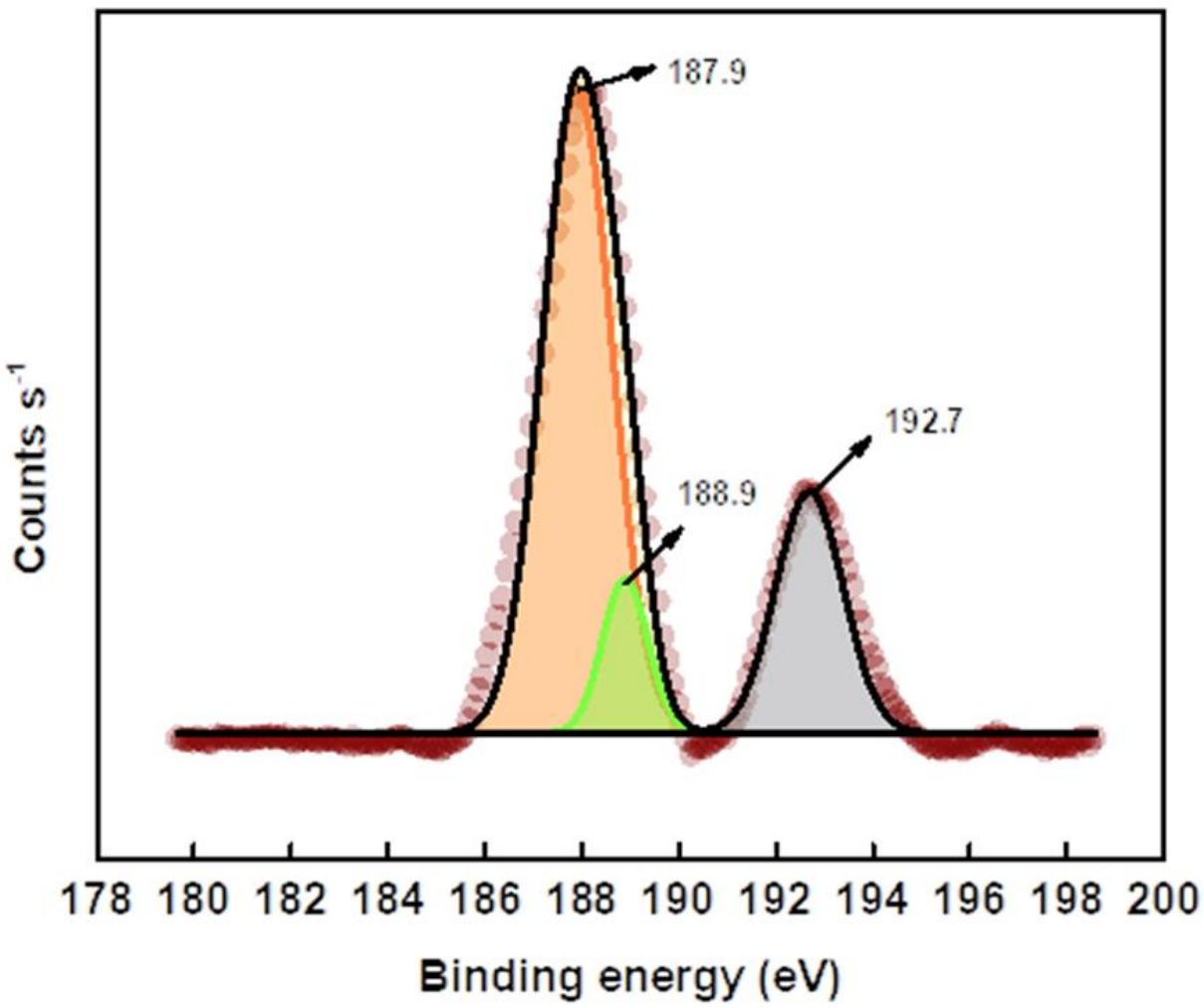

Fig. S4. Core level XPS spectra of B 1s in freestanding borophene in acetone. The left peaks at 187.9 eV and 188.9 eV correspond to B-B bonds, and peak at 192.7 eV corresponds to B-O bond.

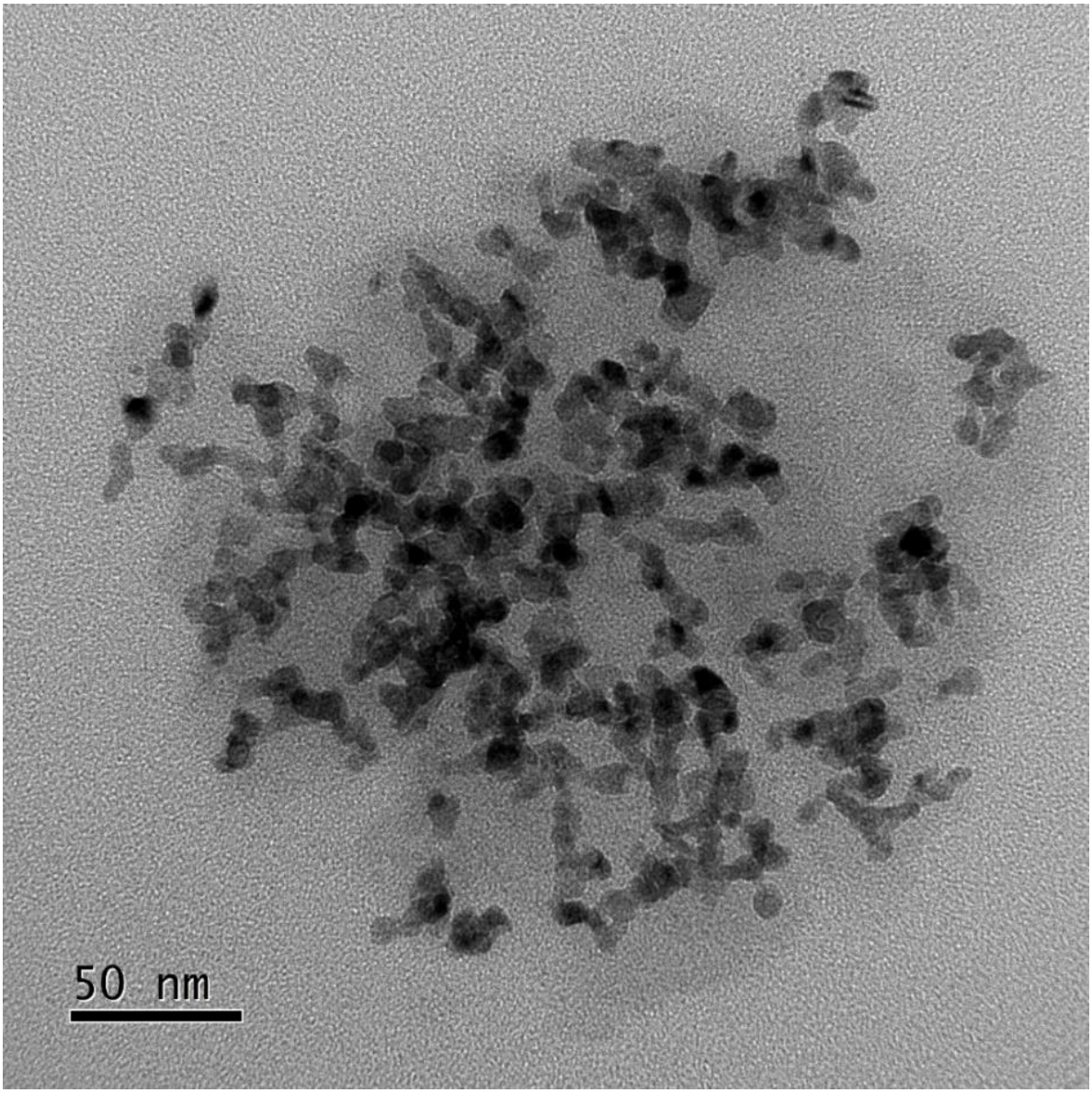

Fig. S5. TEM image of Pd-B catalyst showing plate like structure having size approximately 10 nm resulting in LSPR.

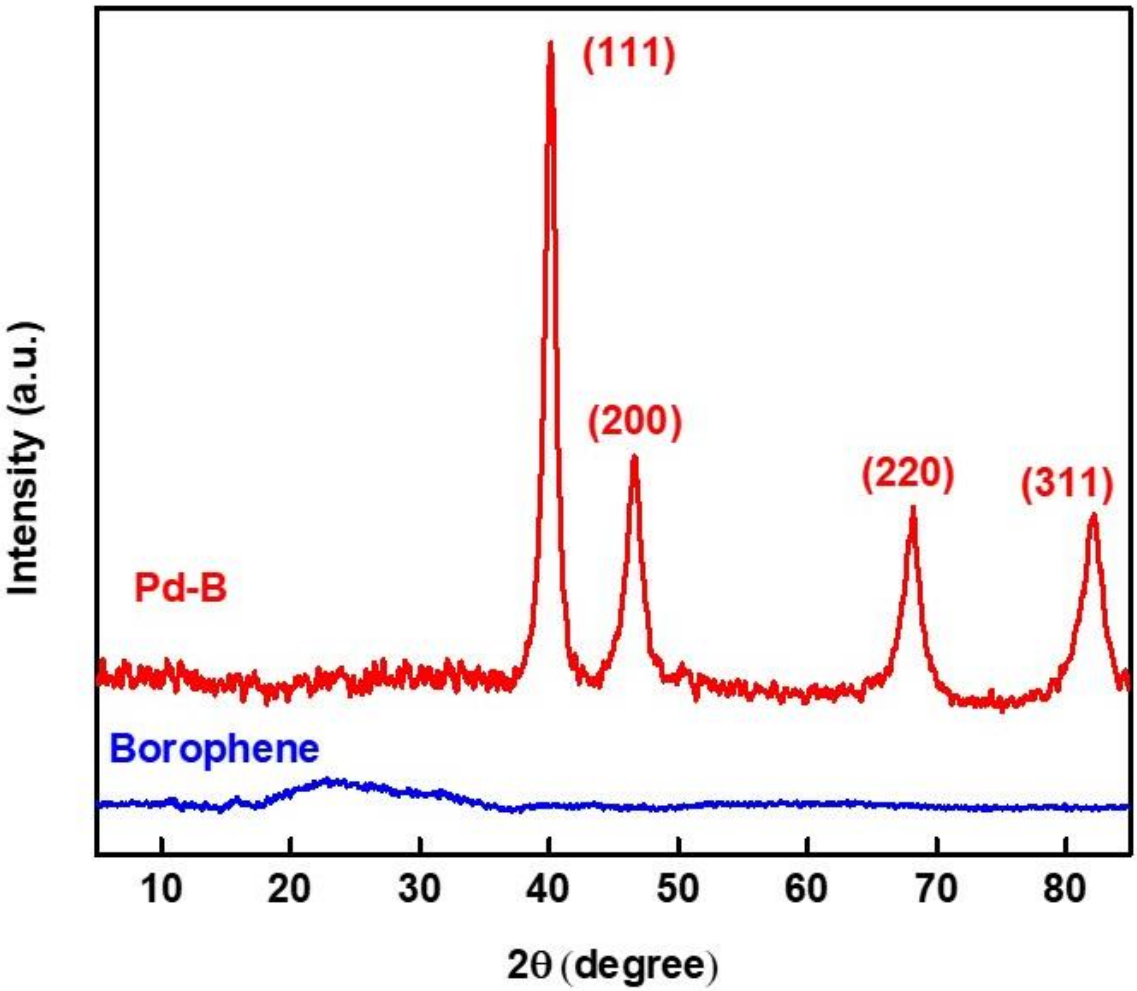

Fig. S6. XRD patterns of borophene and Pd-B.

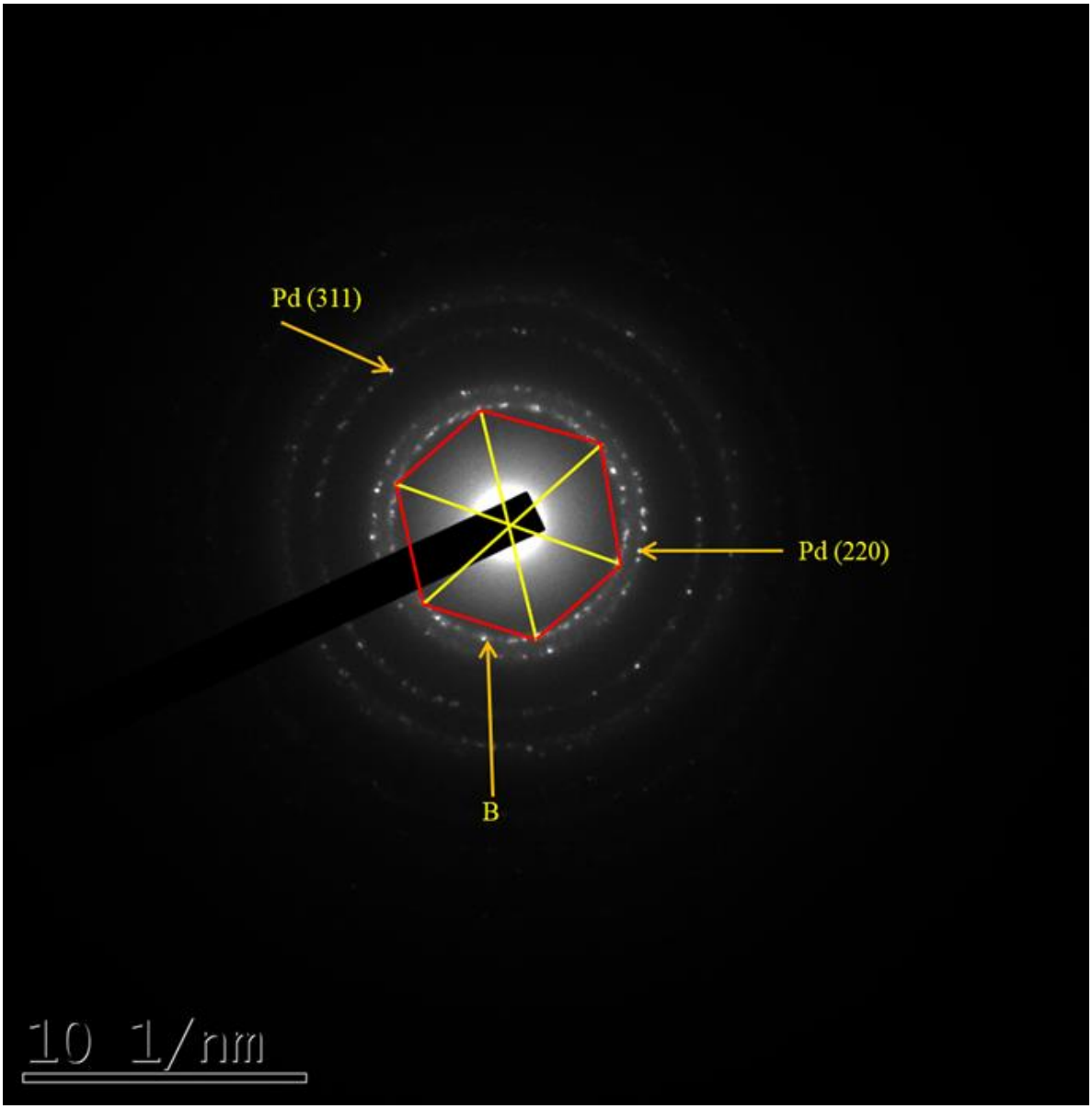

Fig. S7. SAED patterns of Pd-B catalyst showing six-fold symmetry of borophene along with facets of Pd.

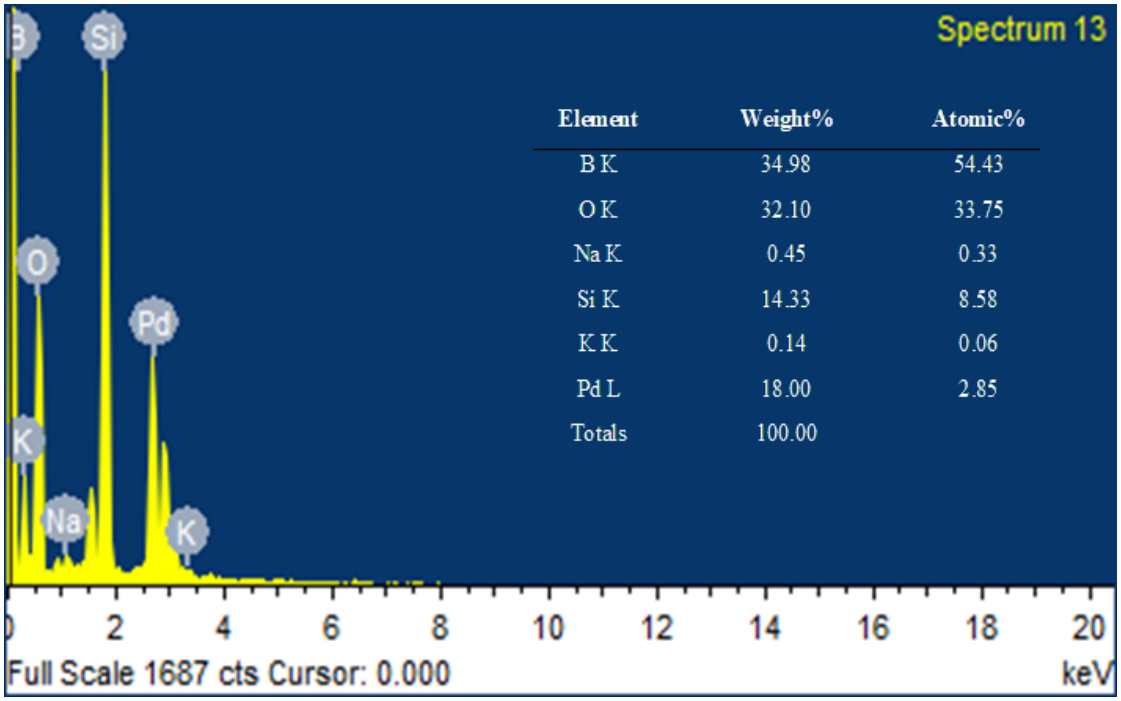

Element	Weight%	Atomic%
B K	34.98	54.43
O K	32.10	33.75
Na K	0.45	0.33
Si K	14.33	8.58
K K	0.14	0.06
Pd L	18.00	2.85
Totals	100.00	

Fig. S8. Elemental analysis of catalyst by EDX, which shows 19.1:1 ratio of B:Pd in optimized catalyst. Silicon came from glass substrate where catalyst was coated for EDX analysis. Other elements came from impurity

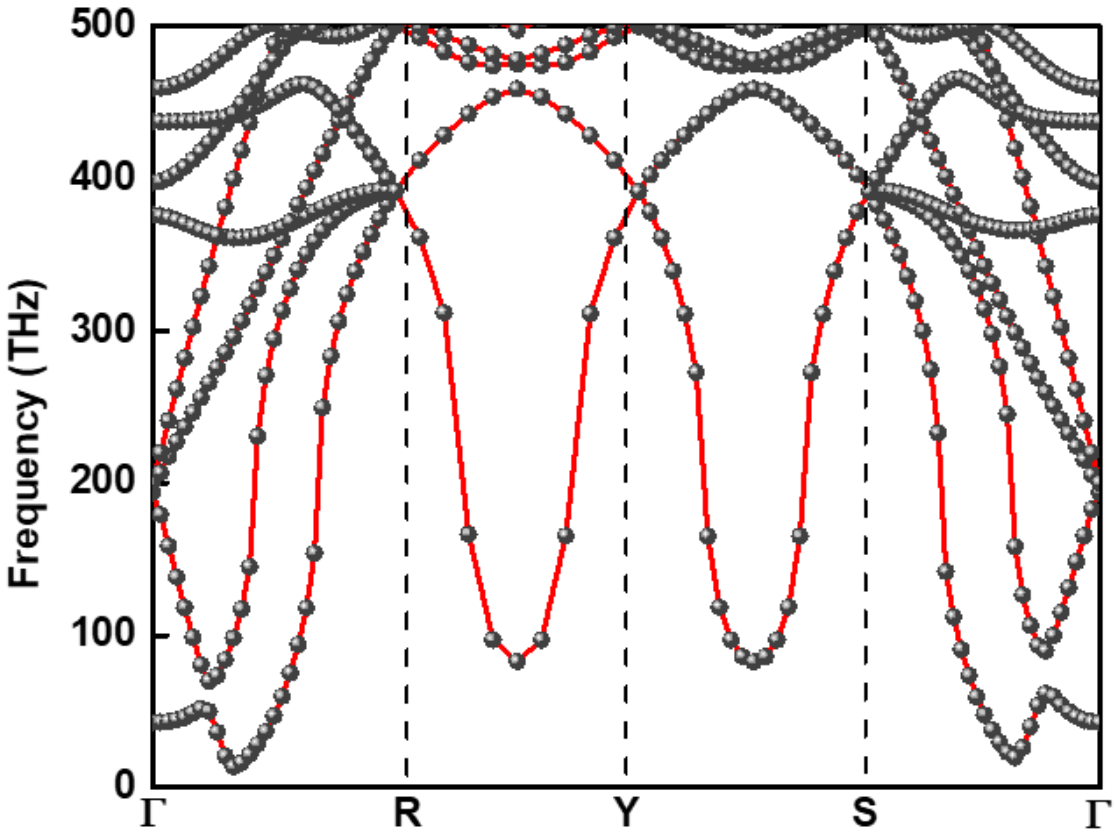

Fig. S9. Phonon dispersion calculation of borophene (β_{12}).

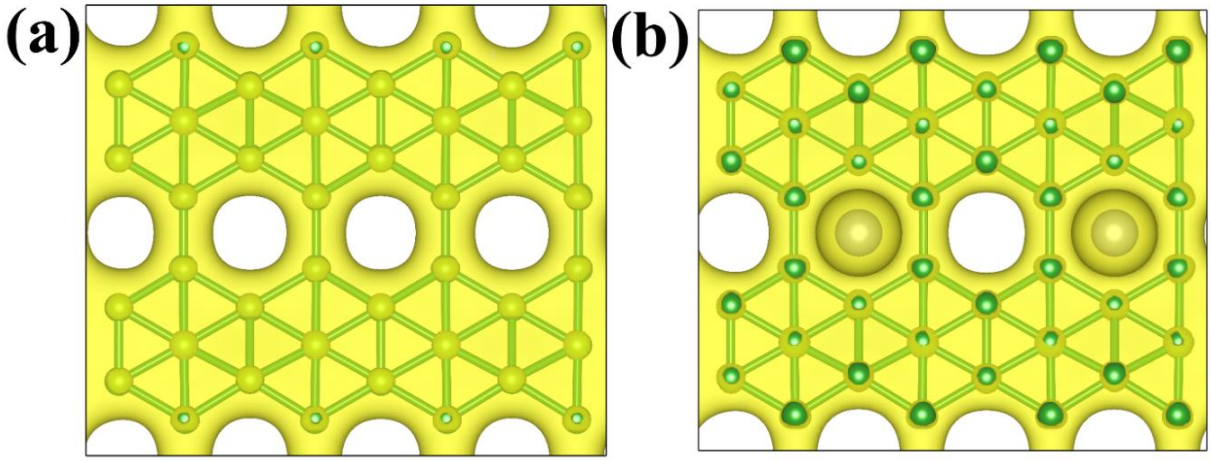

Fig. S10. Charge densities of (a) borophene and (b) Pd-B catalyst used in Bader charge analysis.

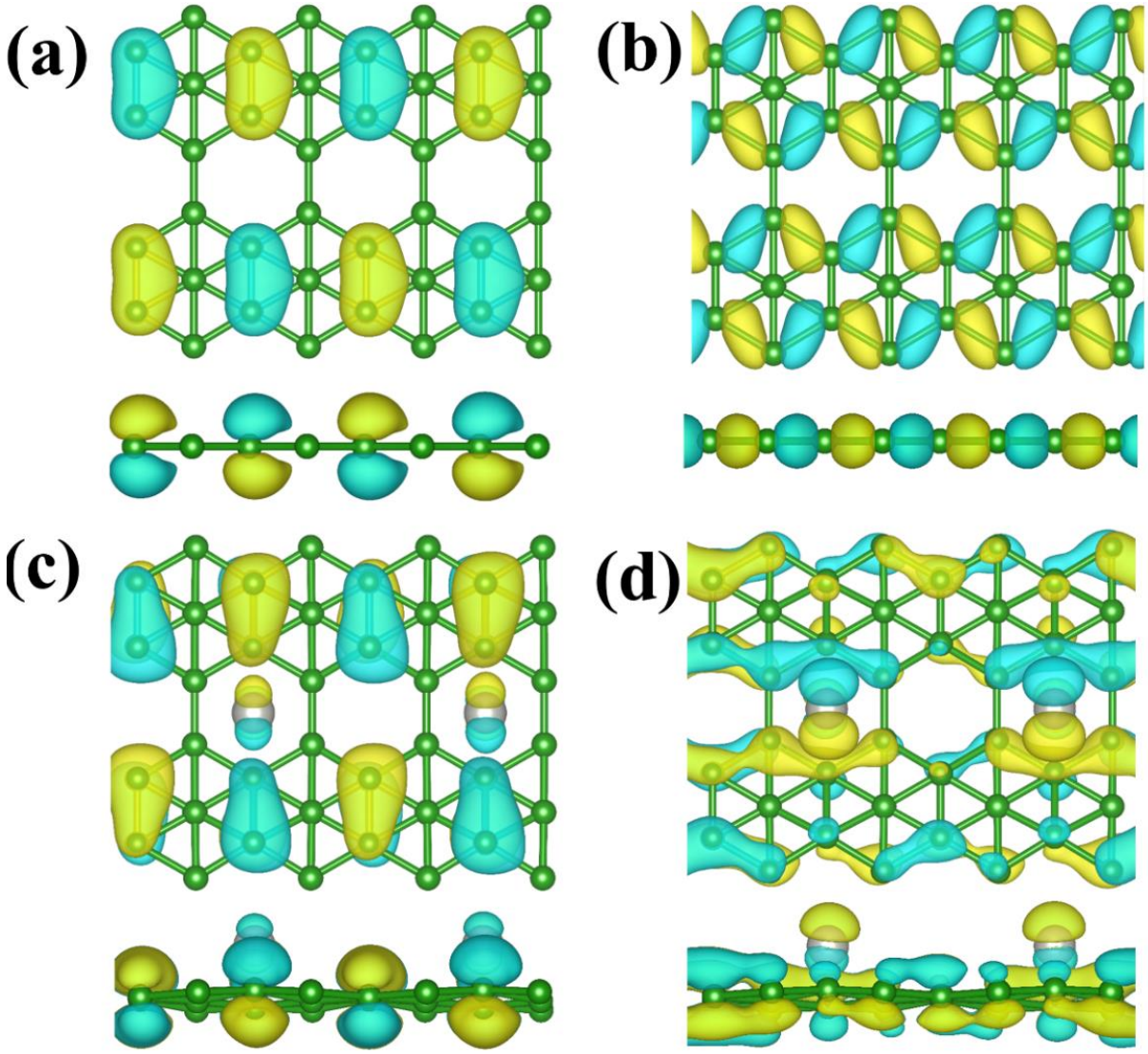

Fig. S11. Charge density distribution (CDD) plot of borophene in (a) valence band and (b) conduction band. CDD plot of Pd-B in (c) valence band, and (d) conduction band.

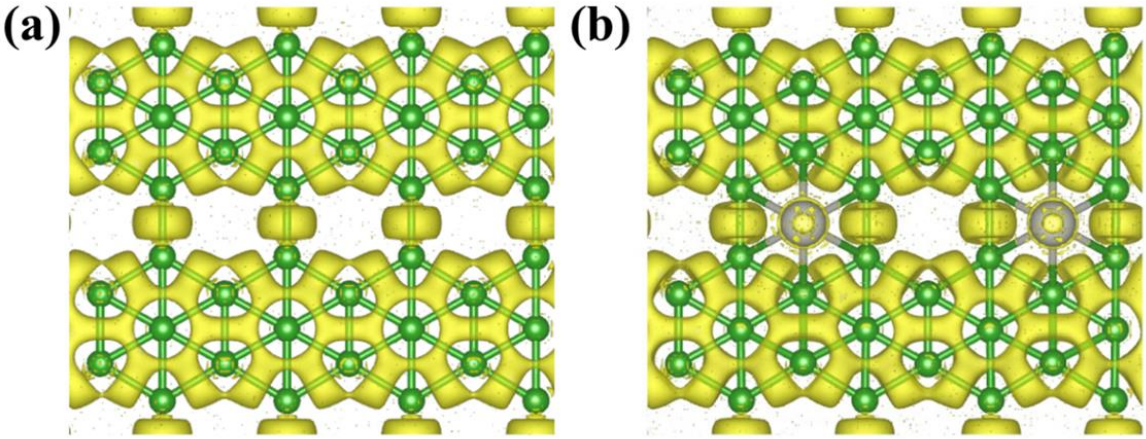

Fig. S12. Electron localization function plot for (a) β_{12} borophene sheet and (b) Pd-B.

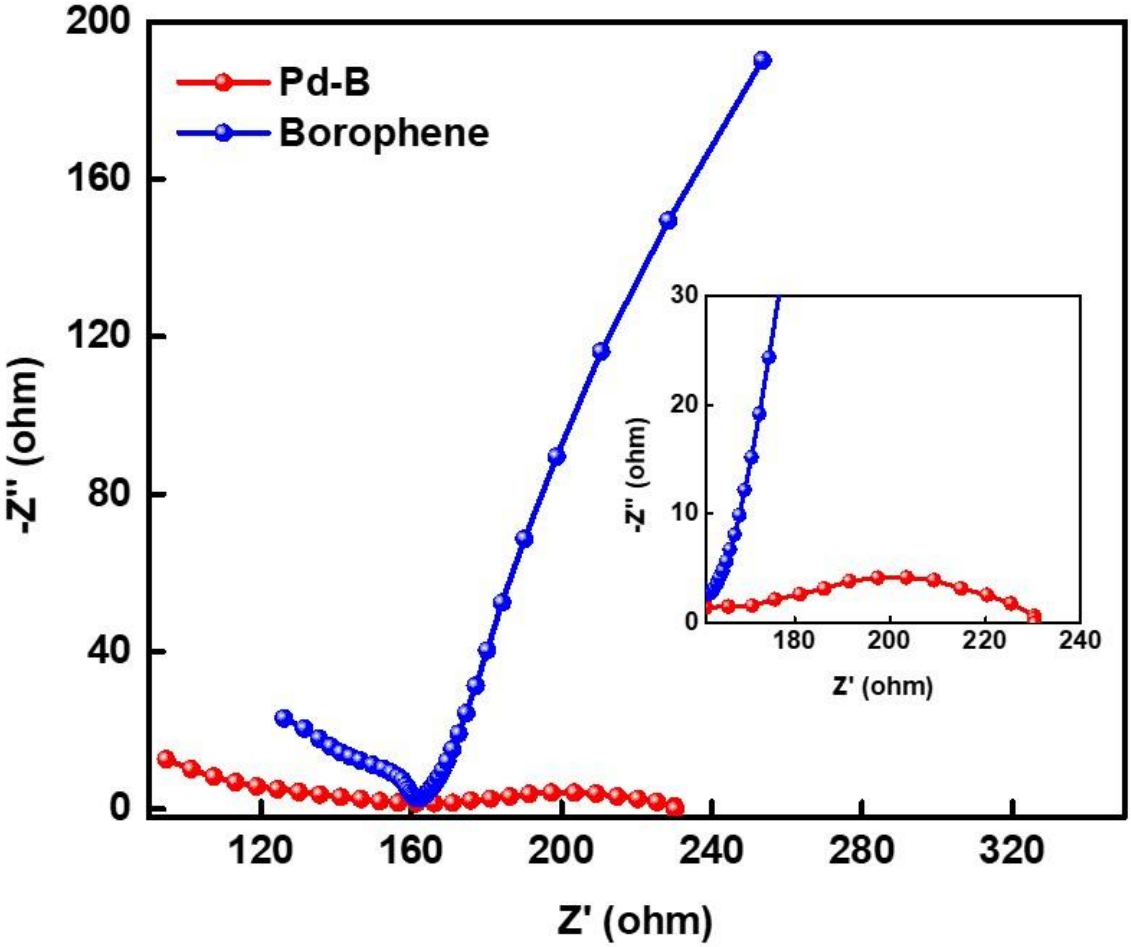

Fig. S13. Nyquist plots of borophene and Pd-B.

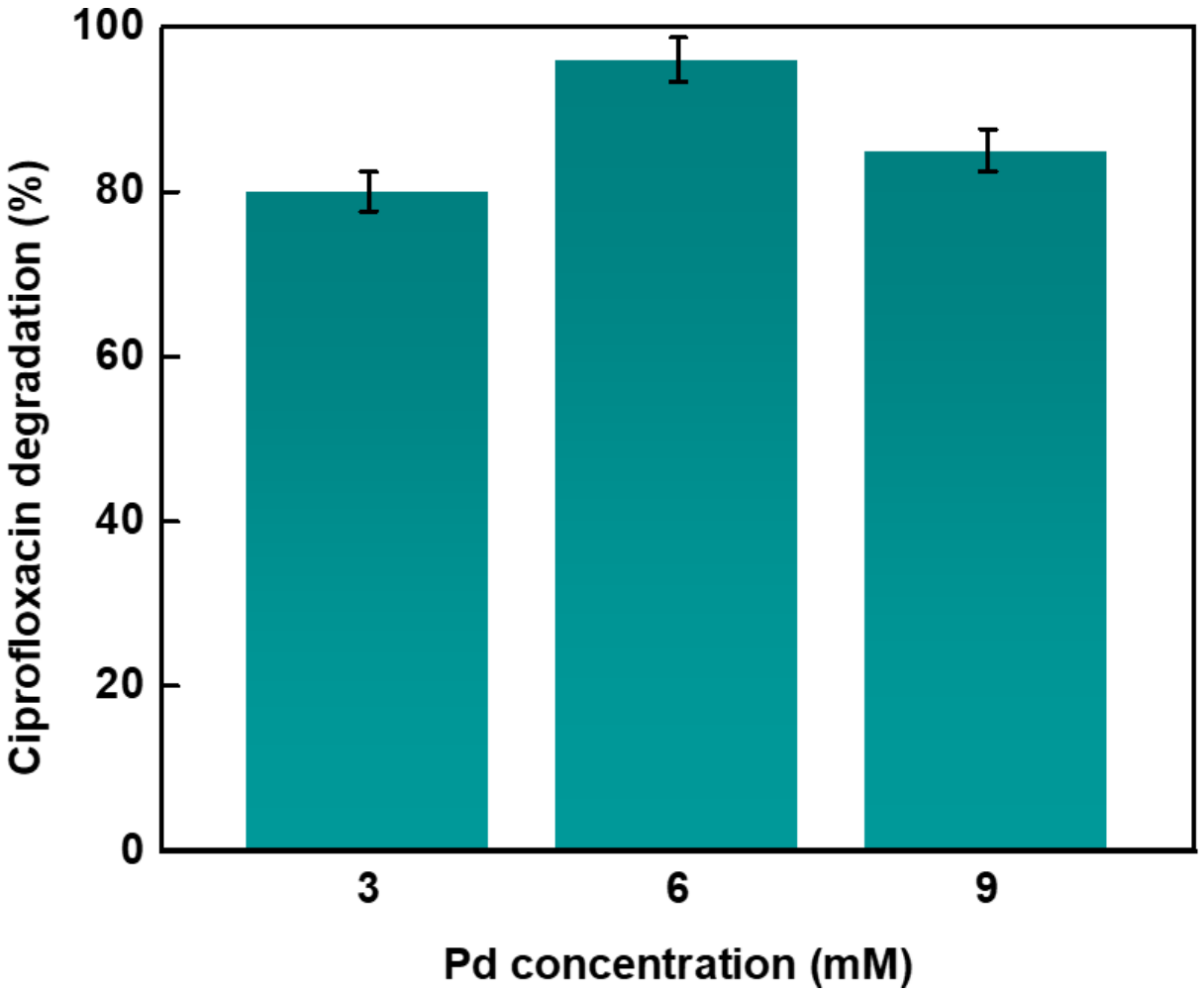

Fig. S14. Effect of palladium concentration used for preparing Pd-B on CIP degradation where highest degradation is achieved with catalyst having B:Pd = 19.1:1.

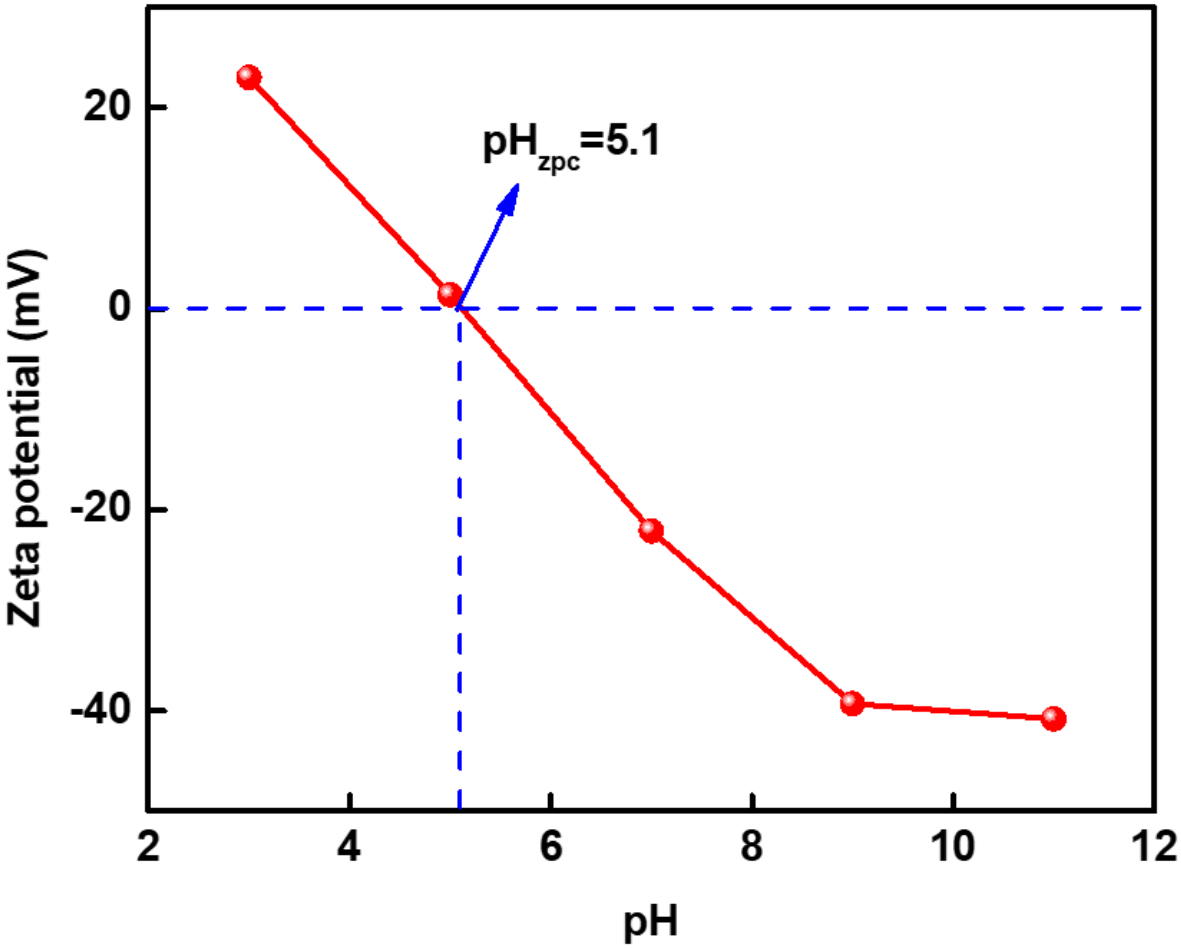

Fig. S15. Variation in zeta potential of Pd-B catalyst at different pH suggests that catalyst surface is positive below pH 5.1, neutral at pH 5.1, and negative above pH 5.1.

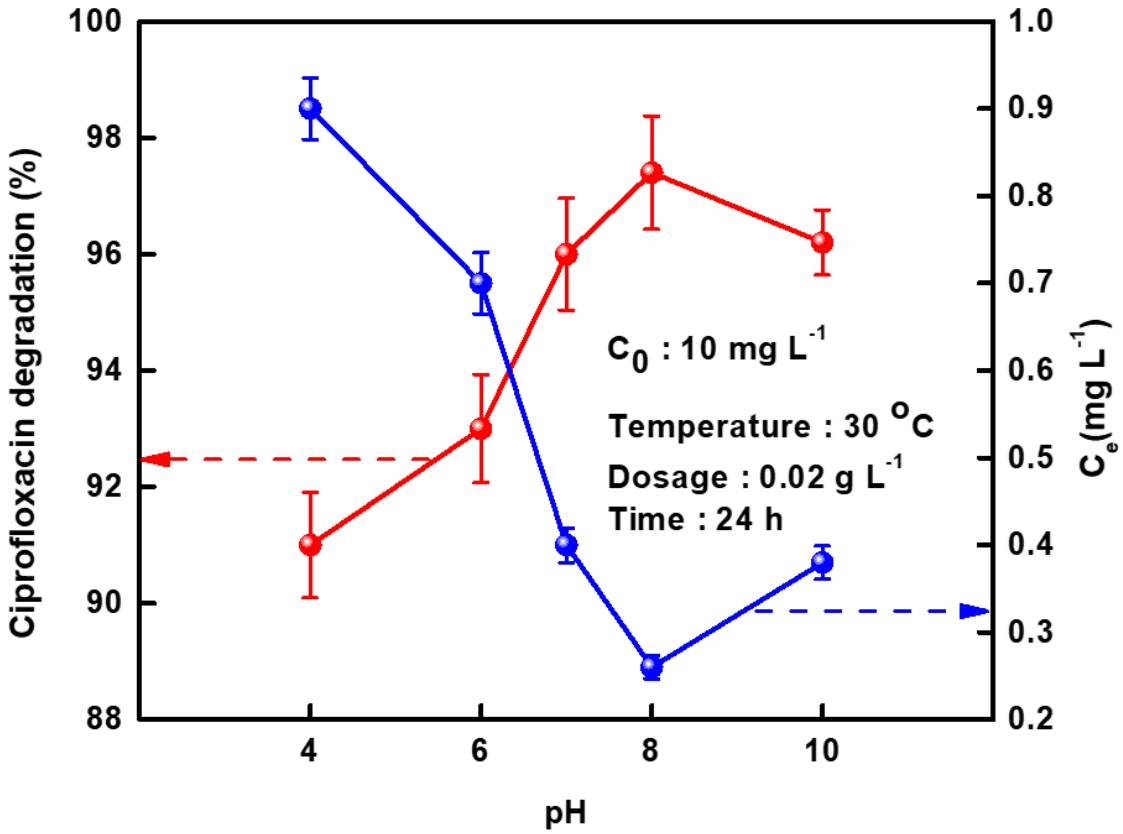

Fig. S16. Effect of solution pH on CIP degradation where maximum degradation is achieved at pH 8.0.

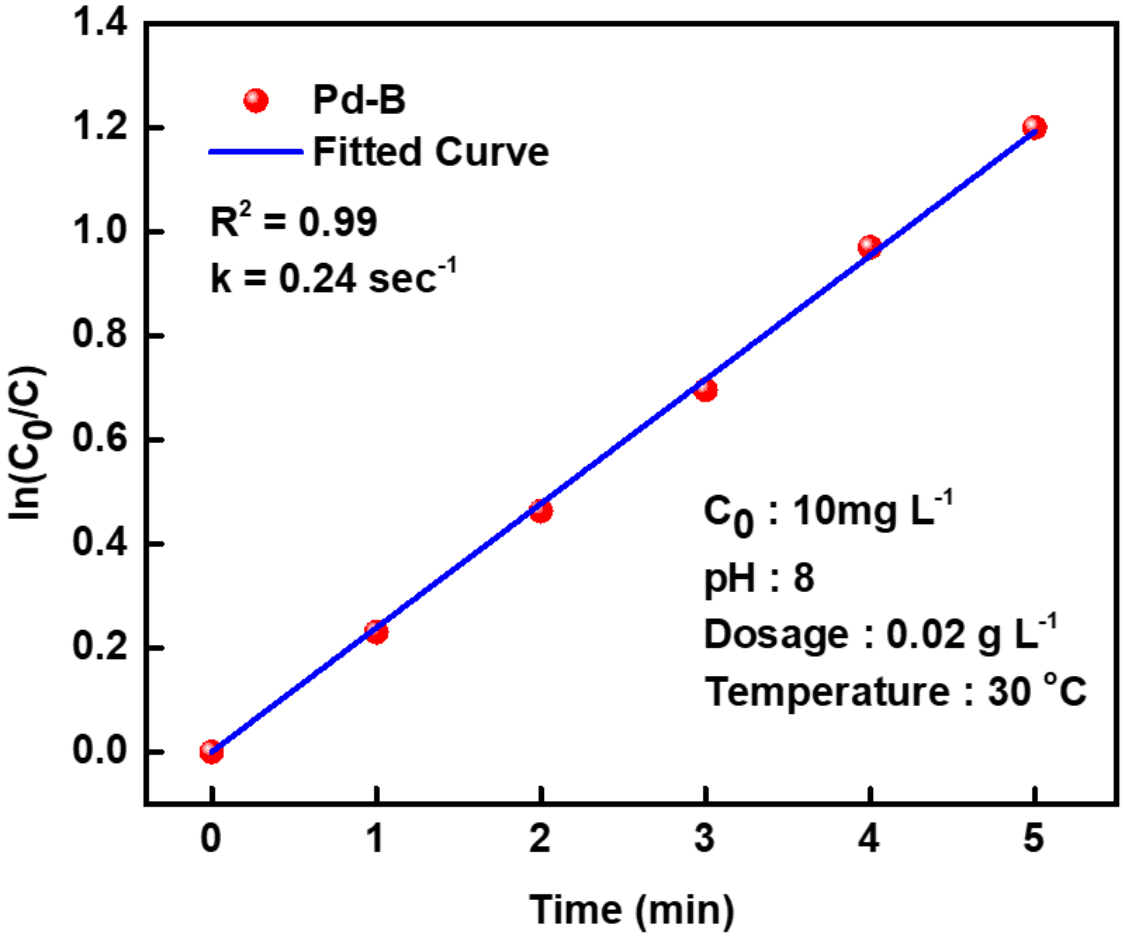

Fig. S17. Pseudo-first-order kinetic plot of degradation of CIP by Pd-B catalyst at optimum pH of 8.0, dose 0.02 g L^{-1}, and temperature of 30ºC.

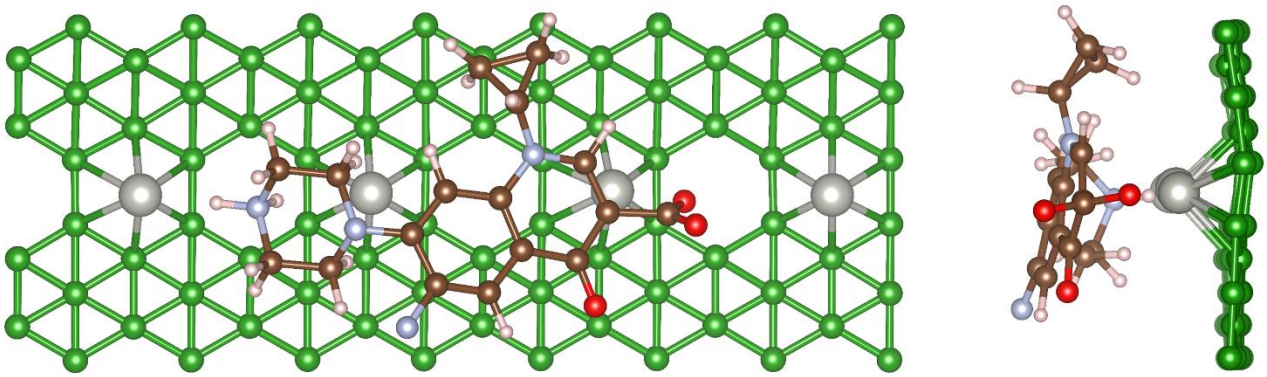

Fig. S18. Geometric structure optimization of drug-Pd-B conjugate by DFT.

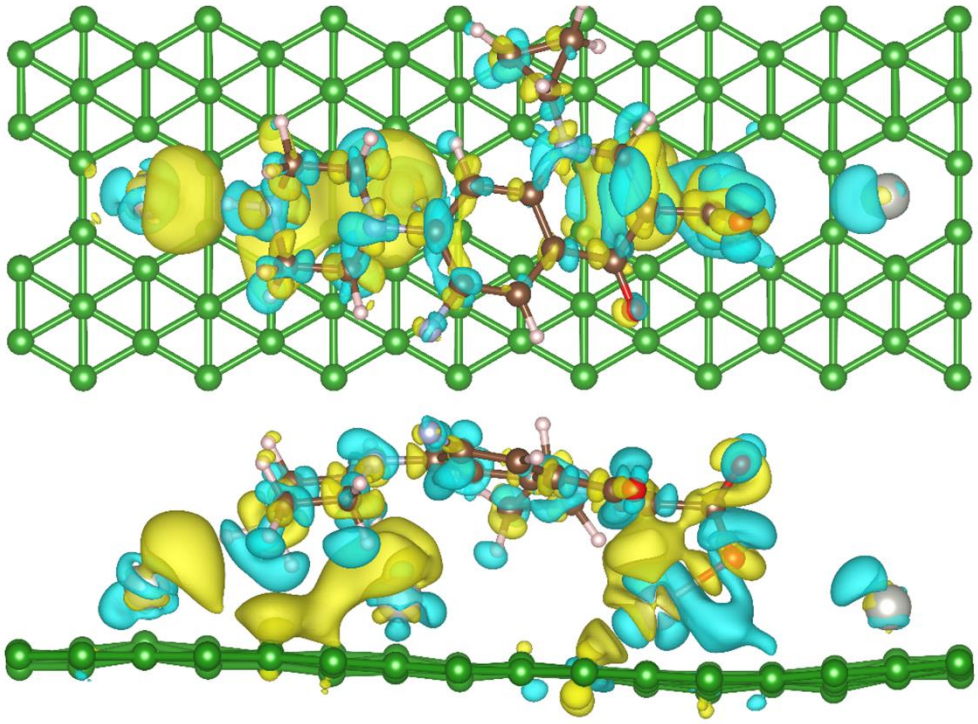

Fig. S19. Charge density difference analysis of drug-catalyst conjugate.

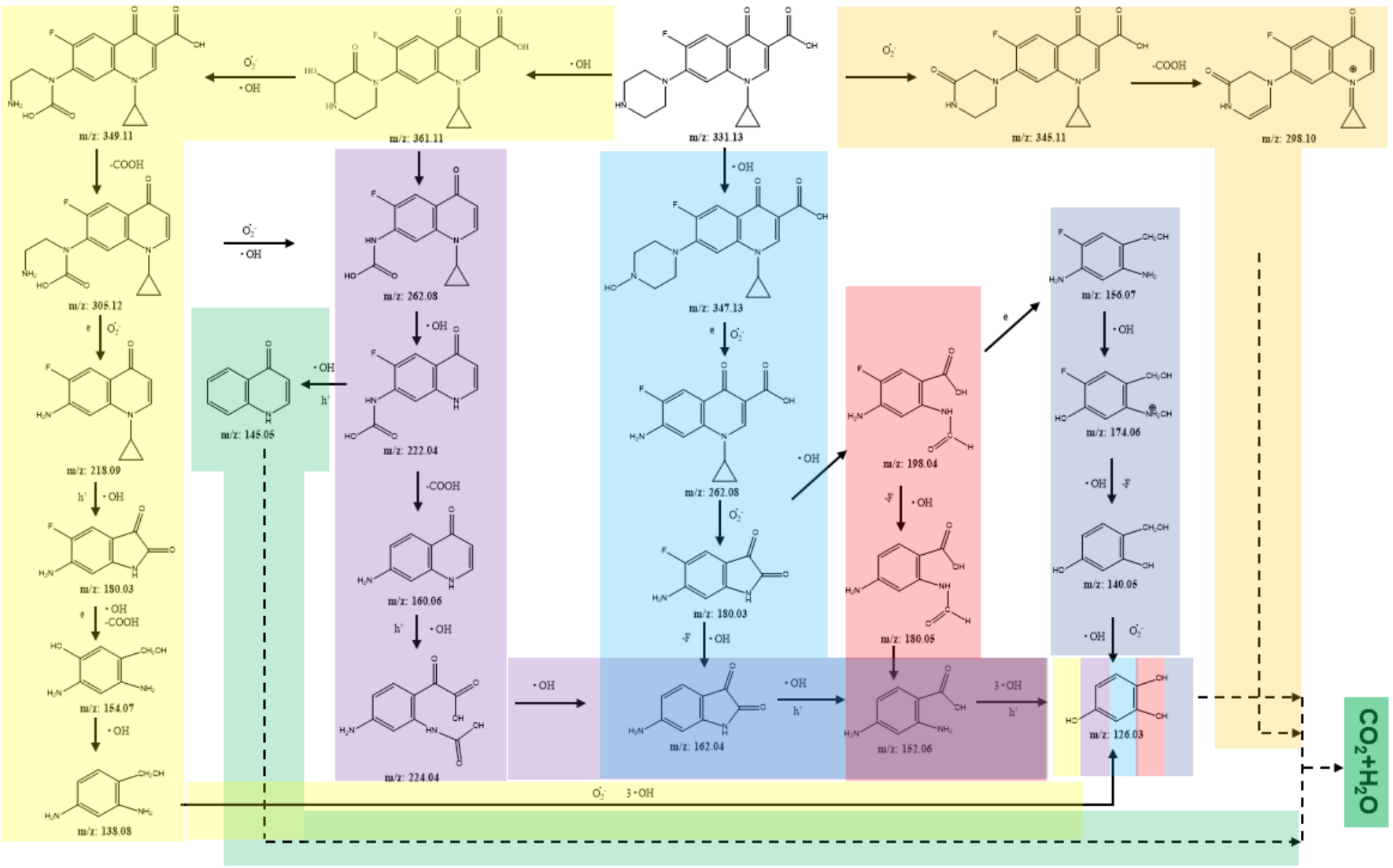

Fig. S20. Detailed reaction mechanism based on the predominant reactive species as observed in scavenging experiment.

Table S1. Details of intermediated generated during CIP degradation.

Product No.	**Chemical Structure**	***m/z***
A	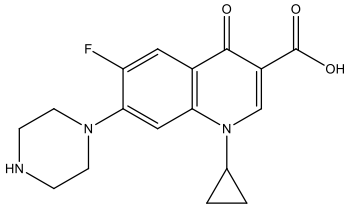 1-cyclopropyl-6-fluoro-4-oxo-7-(piperazin-1-yl)-1,4-dihydroquinoline-3-carboxylic acid (CIP)	331.13
B	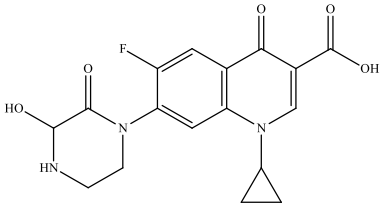 1-cyclopropyl-6-fluoro-7-(3-hydroxy-2-oxopiperazin-1-yl)-4-oxo-1,4-dihydroquinoline-3-carboxylic acid	361.11
C	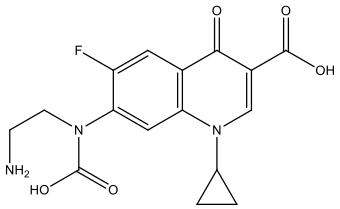 7-((2-aminoethyl)(carboxy)amino)-1-cyclopropyl-6-fluoro-4-oxo-1,4-dihydroquinoline-3-carboxylic acid	349.11
D	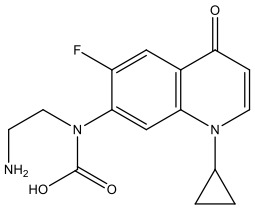 (2-aminoethyl)(1-cyclopropyl-6-fluoro-4-oxo-1,4-dihydroquinolin-7-yl)carbamic acid	305.12

E 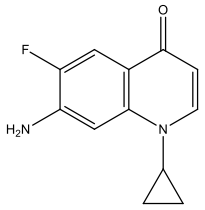 218.09

7-amino-1-cyclopropyl-6-fluoroquinolin-4(1H)-one

F 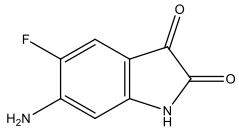 180.03

6-amino-5-fluoroindoline-2,3-dione

G 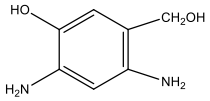 154.07

2,4-diamino-5-(hydroxymethyl)phenol

H 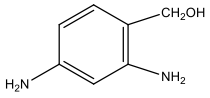 138.08

(2,4-diaminophenyl)methanol

I 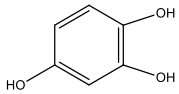 126.03

benzene-1,2,4-triol

J 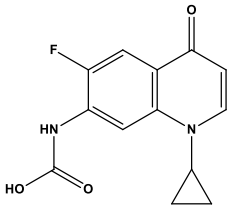 262.08

(1-cyclopropyl-6-fluoro-4-oxo-1,4-dihydroquinolin-7-yl)carbamic acid

K 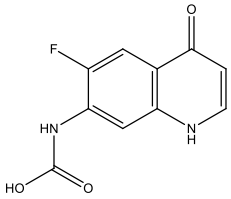 222.04

(6-fluoro-4-oxo-1,4-dihydroquinolin-7-yl)carbamic acid

L 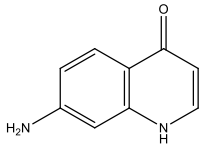 160.06

7-aminoquinolin-4(1H)-one

M 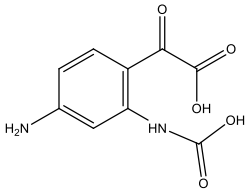 224.04

2-(4-amino-2-(carboxyamino)phenyl)-2-oxoacetic acid

N 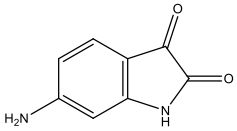 162.04

6-aminoindoline-2,3-dione

O 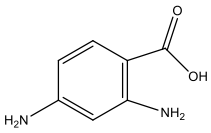 152.06

2,4-diaminobenzoic acid

P 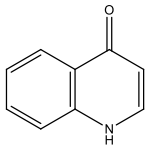 145.05

quinolin-4(1H)-one

Q 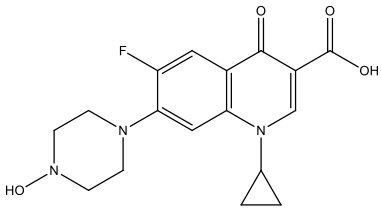 347.13

1-cyclopropyl-6-fluoro-7-(4-hydroxypiperazin-1-yl)-4-oxo-1,4-dihydroquinoline-3-carboxylic acid

R 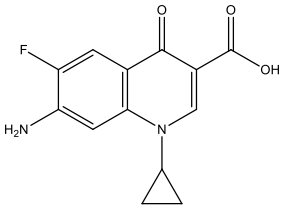 262.08

7-amino-1-cyclopropyl-6-fluoro-4-oxo-1,4-dihydroquinoline-3-carboxylic acid

S 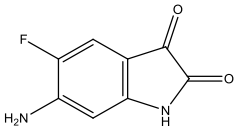 180.03

6-amino-5-fluoroindoline-2,3-dione

T 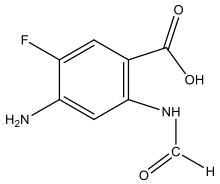 198.04

4-amino-5-fluoro-2-formamidobenzoic acid

U 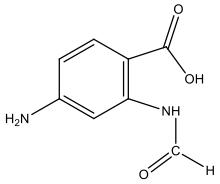 180.05

4-amino-2-formamidobenzoic acid

V 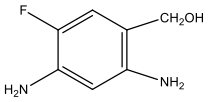 156.07

(2,4-diamino-5-fluorophenyl)methanol

W 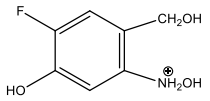 174.06

N-(4-fluoro-5-hydroxy-2-(hydroxymethyl)phenyl)hydroxylammonium

X 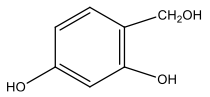 140.05

4-(hydroxymethyl)benzene-1,3-diol

Y 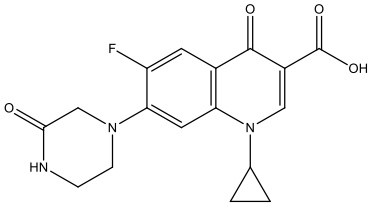 345.11

1-cyclopropyl-6-fluoro-4-oxo-7-(3-oxopiperazin-1-yl)-1,4-dihydroquinoline-3-carboxylic acid

Z 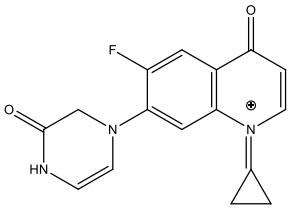 298.10

1-cyclopropylidene-6-fluoro-4-oxo-7-(3-oxo-3,4-dihydropyrazin-1(2H)-yl)-1,4-dihydroquinolin-1-ium

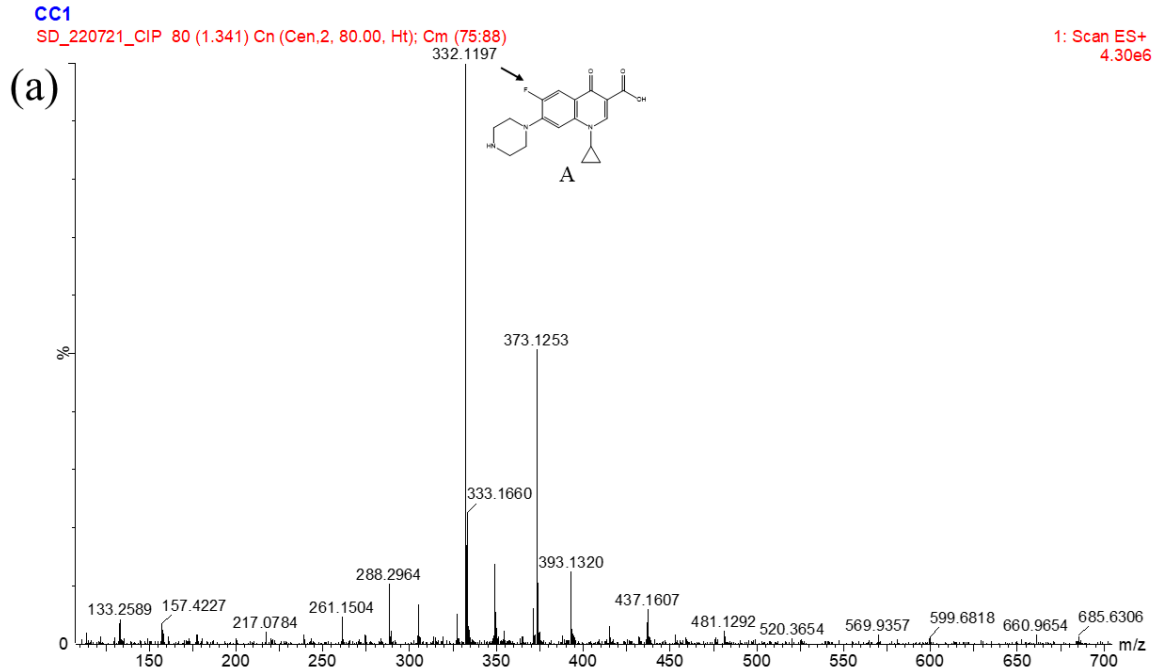
CC1
SD_220721_CIP 80 (1.341) Cn (Cen,2, 80.00, Ht); Cm (75:88)
1: Scan ES+
4.30e6
(a)
A
332.1197
373.1253
333.1660
393.1320
288.2964
133.2589
157.4227
217.0784
261.1504
437.1607
481.1292
520.3654
569.9357
599.6818
660.9654
685.6306
%
m/z

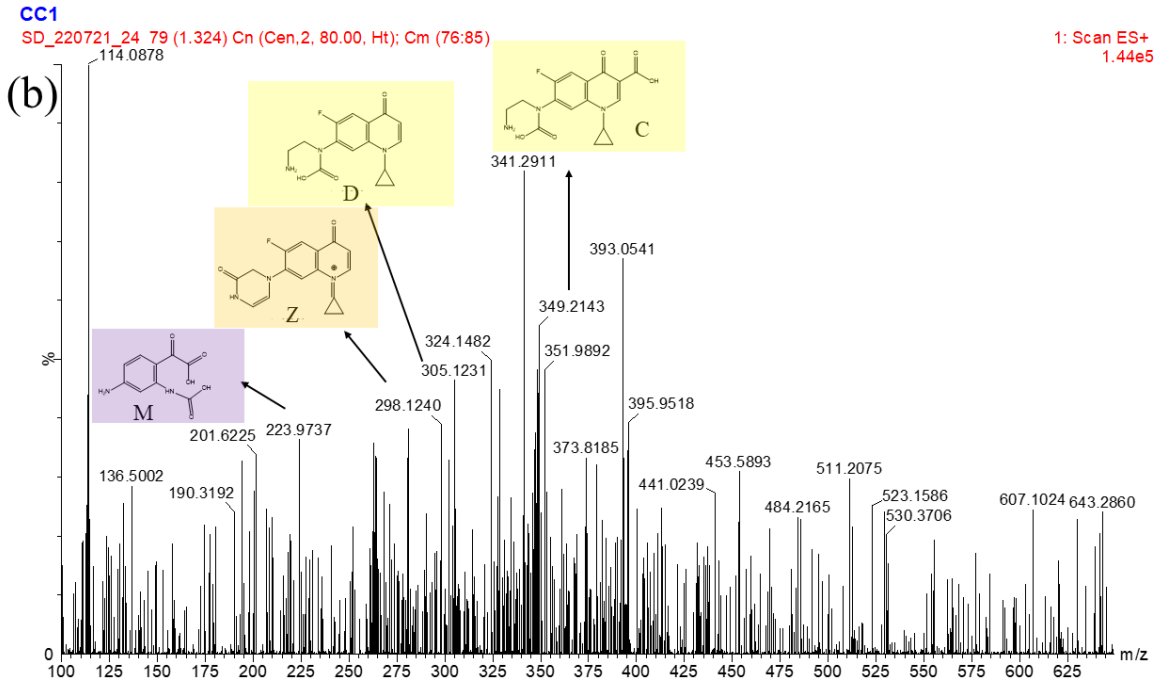
CC1
SD_220721_24 79 (1.324) Cn (Cen,2, 80.00, Ht); Cm (76:85)
1: Scan ES+
1.44e5
(b)
114.0878
C
D
Z
M
341.2911
393.0541
349.2143
324.1482
351.9892
305.1231
298.1240
395.9518
201.6225
223.9737
373.8185
453.5893
136.5002
190.3192
441.0239
511.2075
484.2165
523.1586
530.3706
607.1024
643.2860
%
m/z

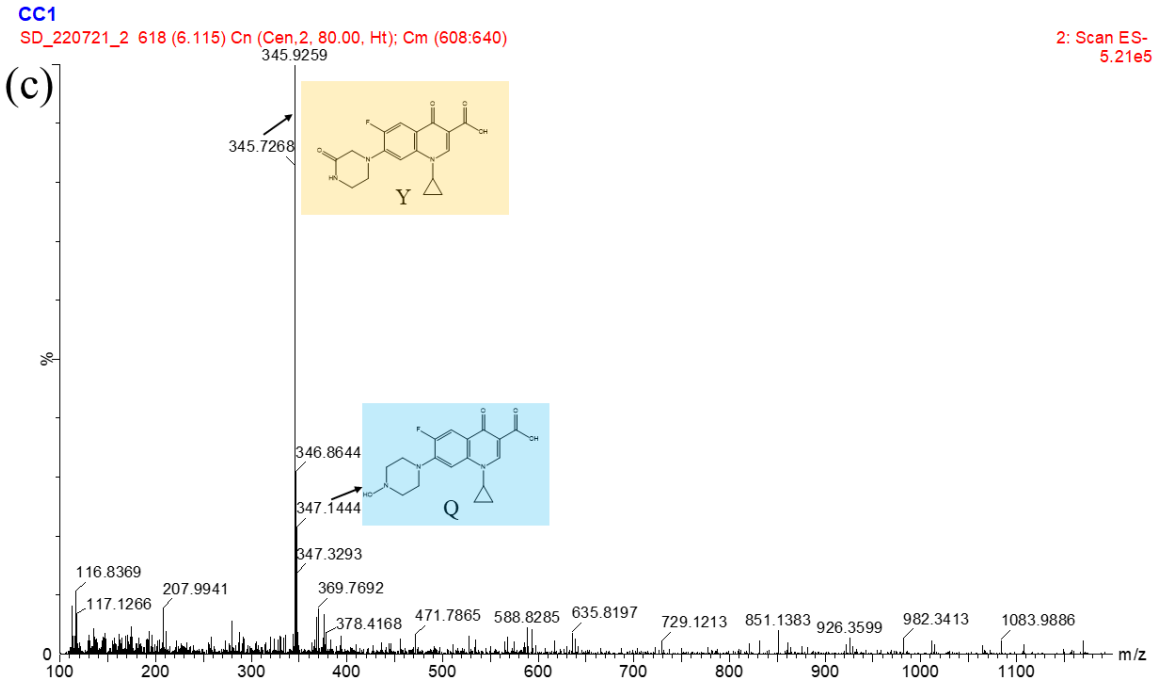
CC1
SD_220721_2 618 (6.115) Cn (Cen,2, 80.00, Ht); Cm (608:640)
2: Scan ES-
5.21e5
(c)
345.9259
345.7268
Y
346.8644
347.1444
Q
347.3293
116.8369
117.1266
207.9941
369.7692
378.4168
471.7865
588.8285
635.8197
729.1213
851.1383
926.3599
982.3413
1083.9886
%
0
100
200
300
400
500
600
700
800
900
1000
1100
m/z

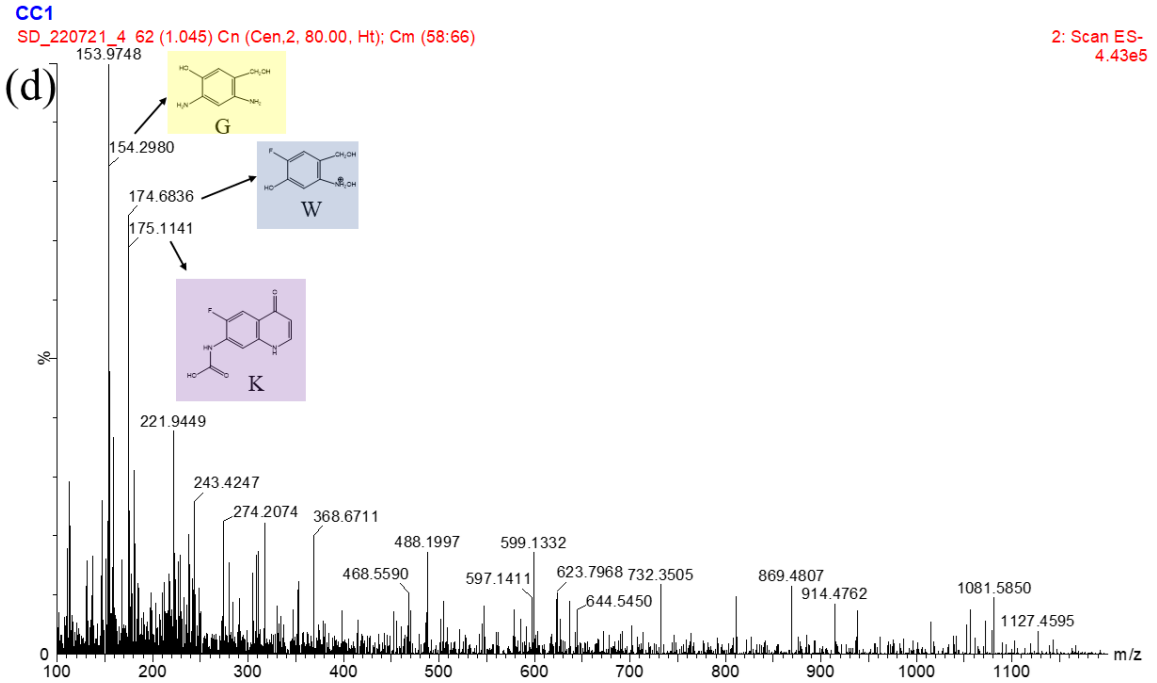
CC1
SD_220721_4 62 (1.045) Cn (Cen,2, 80.00, Ht); Cm (58:66)
2: Scan ES-
4.43e5
(d)
153.9748
G
154.2980
174.6836
W
175.1141
K
221.9449
243.4247
274.2074
368.6711
488.1997
599.1332
468.5590
597.1411
623.7968
732.3505
869.4807
914.4762
1081.5850
644.5450
1127.4595
%
0
100
200
300
400
500
600
700
800
900
1000
1100
m/z

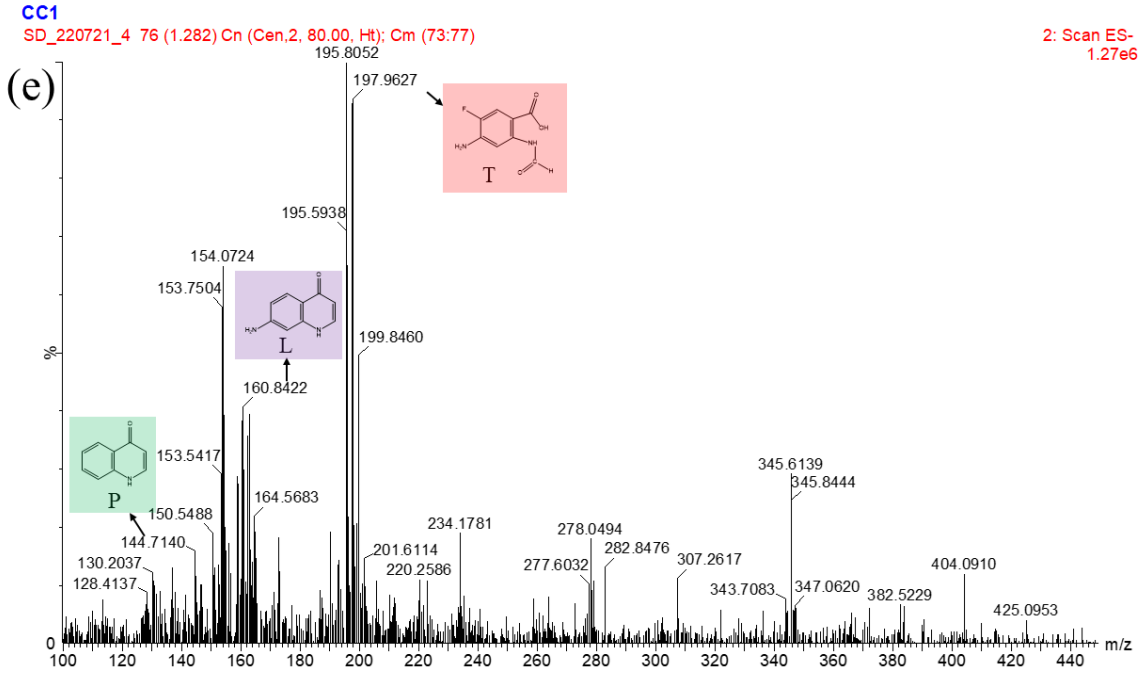
CC1
SD_220721_4 76 (1.282) Cn (Cen,2, 80.00, Ht); Cm (73:77)
2: Scan ES-
1.27e6
(e)
195.8052
197.9627
T
195.5938
154.0724
153.7504
L
199.8460
160.8422
P
153.5417
164.5683
150.5488
144.7140
130.2037
128.4137
234.1781
201.6114
220.2586
278.0494
277.6032
282.8476
307.2617
345.6139
345.8444
343.7083
347.0620
382.5229
404.0910
425.0953
%
0
100 120 140 160 180 200 220 240 260 280 300 320 340 360 380 400 420 440
m/z

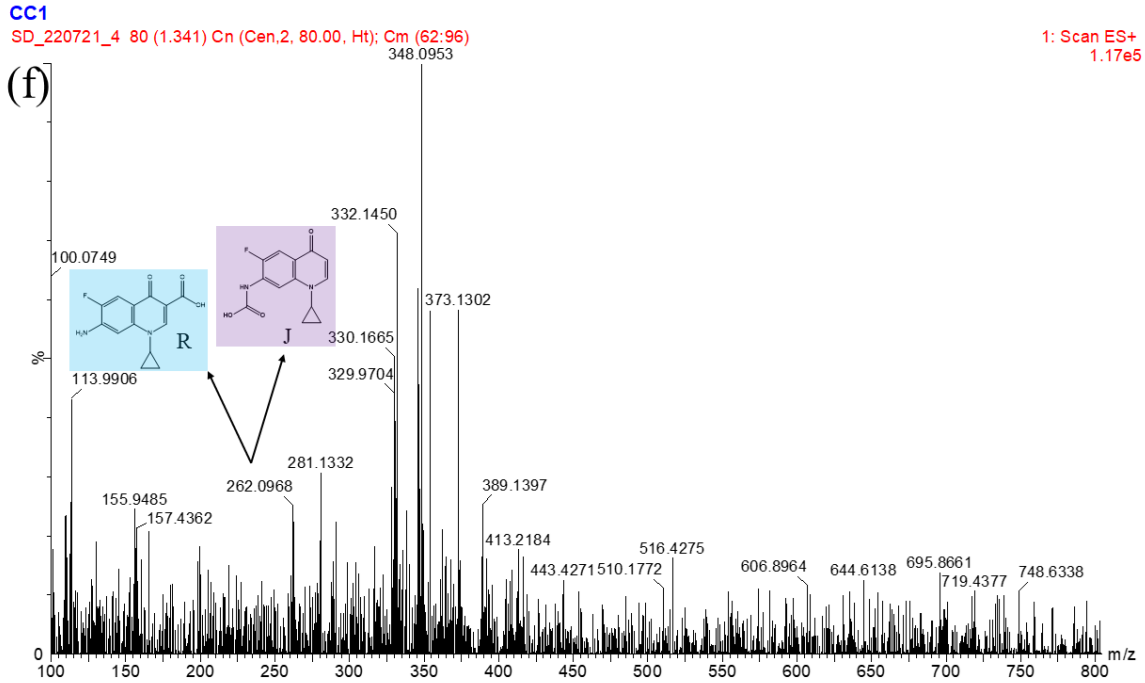
CC1
SD_220721_4 80 (1.341) Cn (Cen,2, 80.00, Ht); Cm (62:96)
1: Scan ES+
1.17e5
(f)
348.0953
332.1450
100.0749
R
J
373.1302
330.1665
329.9704
113.9906
281.1332
262.0968
389.1397
155.9485
157.4362
413.2184
443.4271
510.1772
516.4275
606.8964
644.6138
695.8661
719.4377
748.6338
%
0
100 150 200 250 300 350 400 450 500 550 600 650 700 750 800
m/z

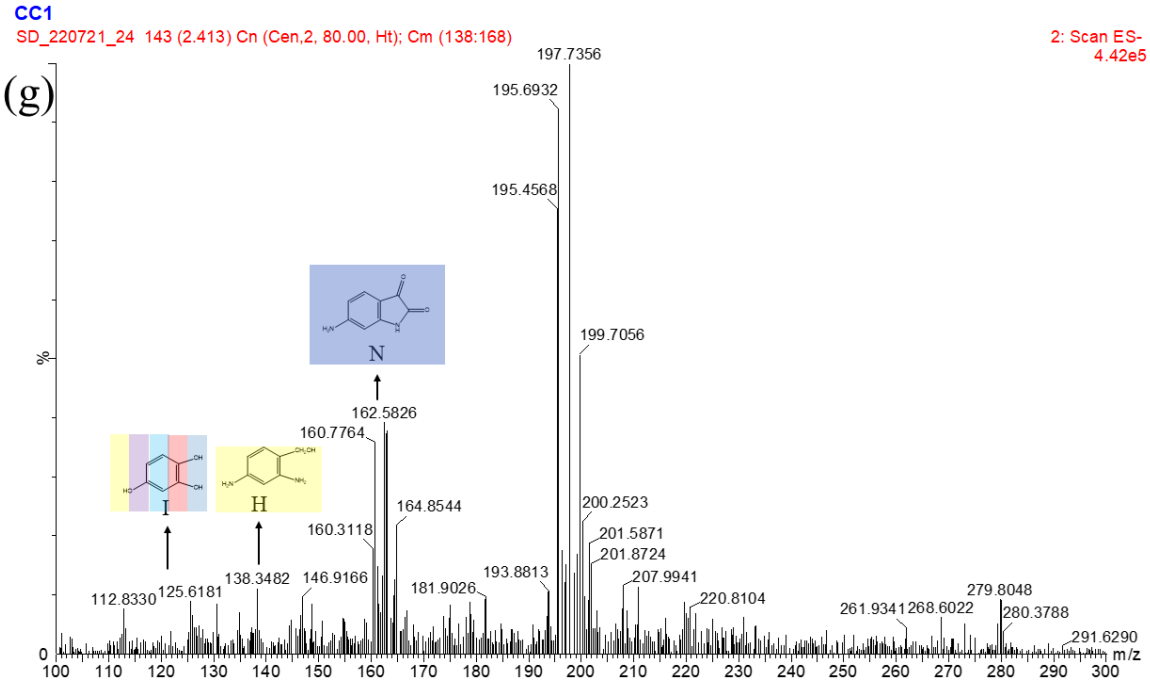
CC1
SD_220721_24 143 (2.413) Cn (Cen,2, 80.00, Ht); Cm (138:168)
2: Scan ES-
4.42e5
(g)
197.7356
195.6932
195.4568
199.7056
N
162.5826
160.7764
I
H
164.8544
160.3118
200.2523
201.5871
201.8724
193.8813
207.9941
138.3482
146.9166
181.9026
112.8330
125.6181
220.8104
261.9341
268.6022
279.8048
280.3788
291.6290
%
m/z

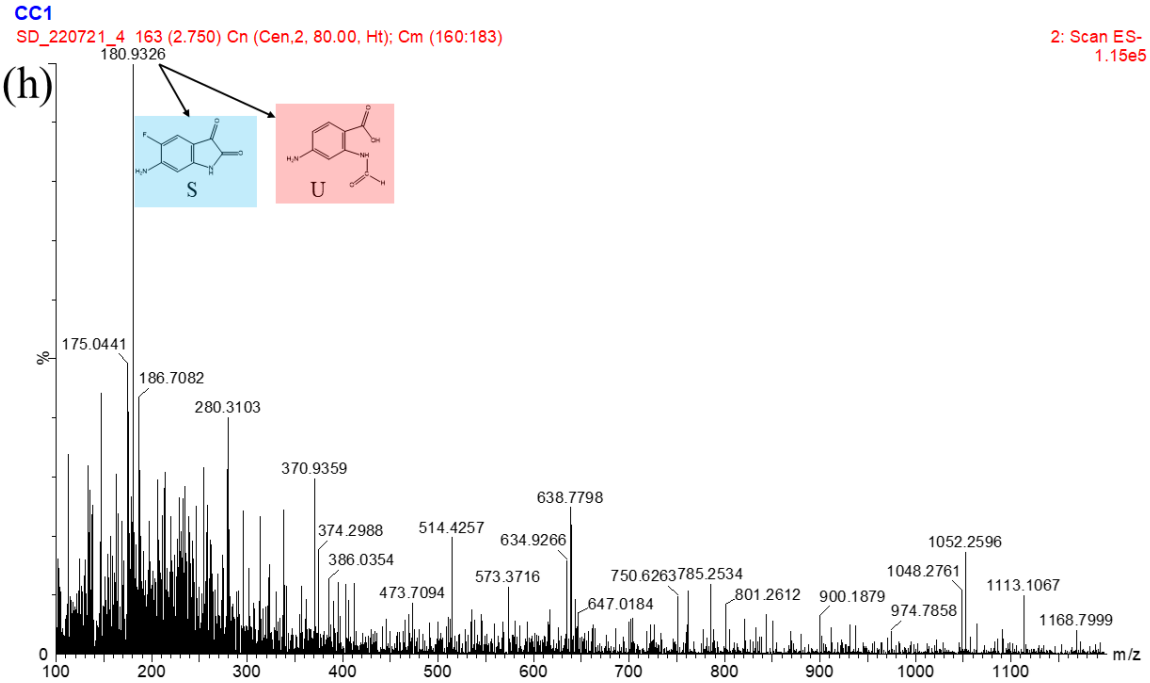
CC1
SD_220721_4 163 (2.750) Cn (Cen,2, 80.00, Ht); Cm (160:183)
2: Scan ES-
1.15e5
(h)
180.9326
S
U
175.0441
186.7082
280.3103
370.9359
638.7798
374.2988
514.4257
634.9266
386.0354
1052.2596
1048.2761
573.3716
750.6263
785.2534
1113.1067
473.7094
801.2612
900.1879
647.0184
974.7858
1168.7999
%
m/z

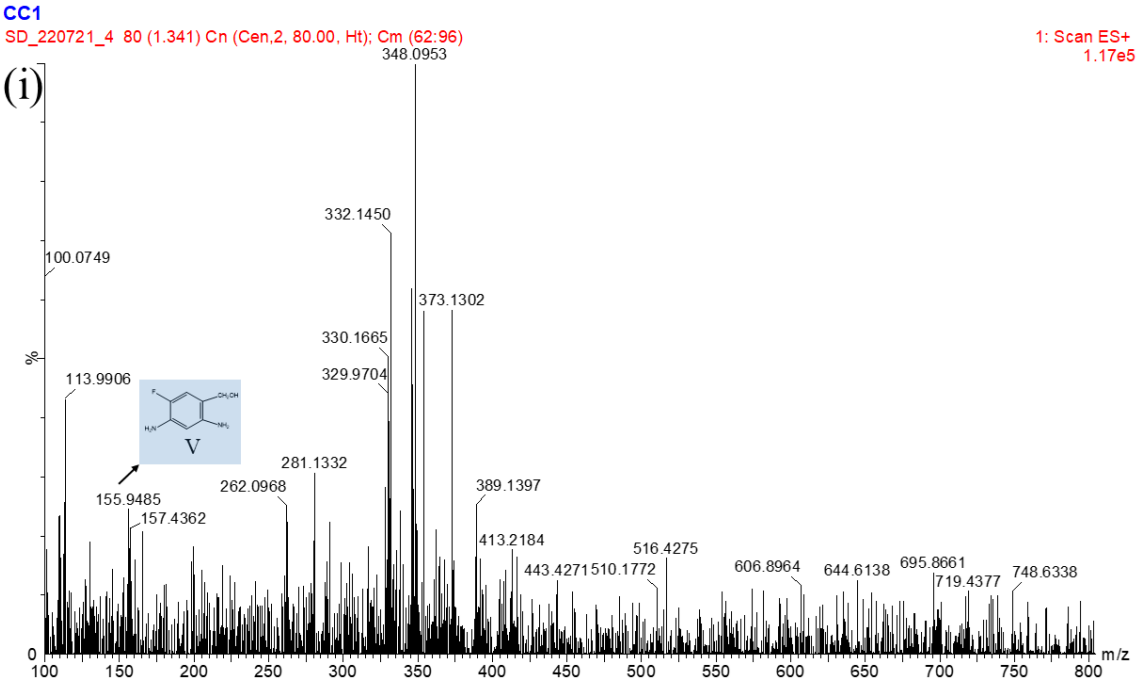

Fig. S21. (a-i) LC-MS spectra of different intermediates generated in CIP degradation process.

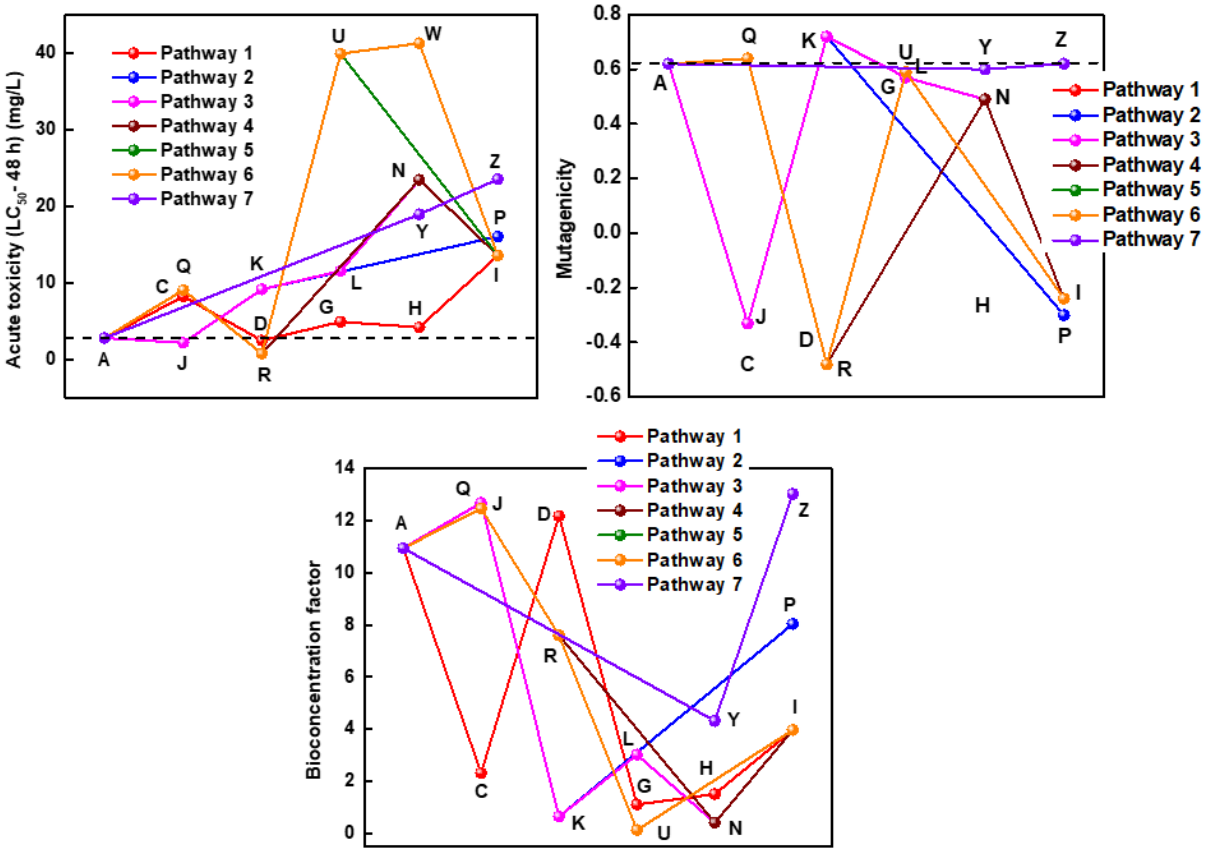

Fig. S22. (a) Acute toxicity, (b) Mutagenicity, and (c) Bioconcentration factor of CIP and its degradation intermediates in different proposed pathways.

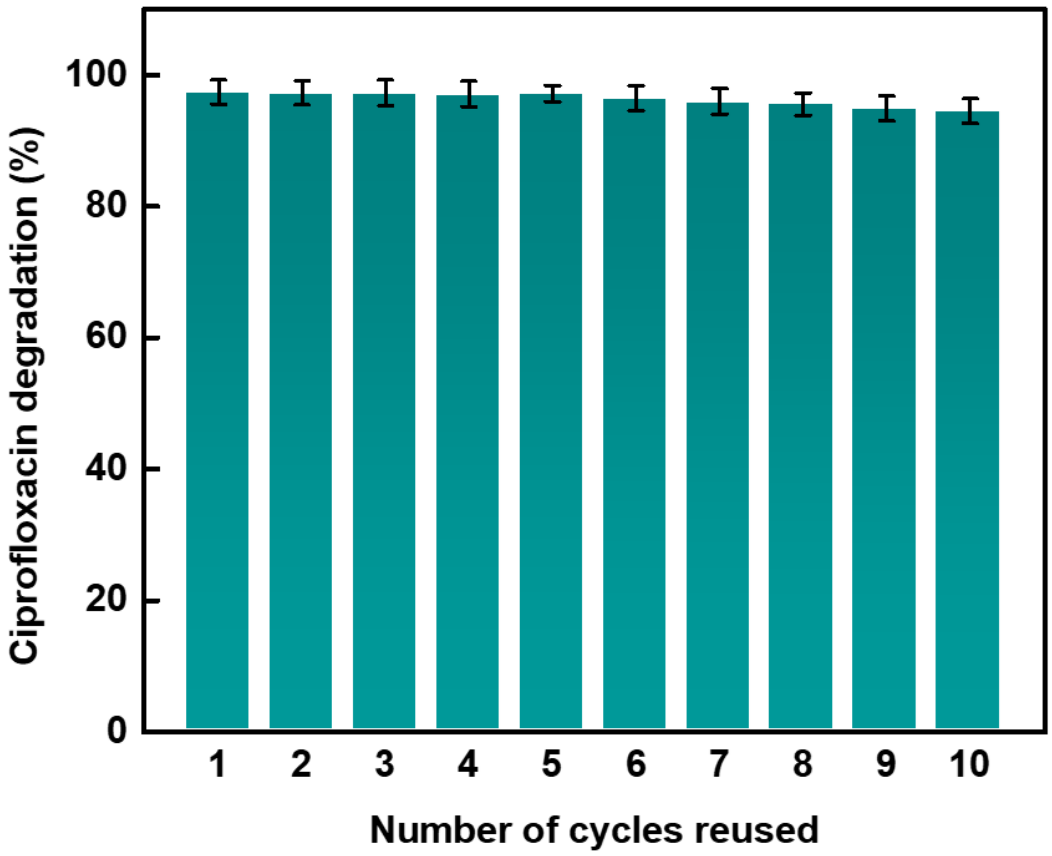

Fig. S23. Effect of the number of cycles reused on CIP degradation efficiency.

S3. Comparison with other photocatalysts

Researches have reported several photocatalysts with efficient degradation capacity of CIP. A brief comparison has been presented in **Table S2**.

Table S2. Comparison of CIP degradation efficiency of different photocatalysts.

Photocatalyst	Dose ($g\ L^{-1}$)	CIP conc. ($mg\ L^{-1}$)	Source	Intensity	Degradation efficiency	Ref.
$WO_3/CdWO_4$	0.57	20	500 W Xe lamp	100 mW cm^{-2}	93.4% (90 min)	[1]
ZnO/CD NCs	0.6	12	Natural sunlight	221 W m^{-2}	98% (110 min)	[2]
Ce/Zr MOF	1.0	20	300 W Xe lamp (λ>420 nm)	-	90.8% (60 min)	[3]
NiAl LDH/Fe_3O_4–RGO	0.25	10	500 W Xe lamp (λ>420 nm)	-	91.36% (150 min)	[4]
AgBr/Ag@Ag_2O/Ag_2CO_3	1	10	300 W Xe lamp (λ>420 nm)	-	89.3% (60 min)	[5]
Exfoliated B-doped g-C_3N_4	1	10	Solar light	-	90% (60 min)	[6]
2D–2D ZnO/N doped g-C_3N_4	0.1	10	300 W Xe lamp (λ>420 nm)	-	64.4% (30 min)	[7]
Ag–TiO_2 NPs	0.3	3	Simulated natural solar light (λ: 400 nm-1100 nm)	98 W m^{-2}	92% (240 min)	[8]
MoS_2/CeO_2	0.5	10	250 W Xe lamp (λ>420 nm)	-	88.5% (120 min)	[9]
porous CN	1	10	500 W Xe lamp (λ>420 nm)	-	79% (110 min)	[10]
2D $Bi_2O_2CO_3$	1	10	300 W Xe lamp	-	76.8% (60 min)	[11]
TiO_2 (Degussa P25)	0.5	33.1	Oriel 459 WO_3^- free Xe arc lamp with cut-off filter	-	100% (60 min, λ>400 nm) 88% (60 min, λ>420 nm)	[12]

					<5% (60 min, λ>450 nm)	
TiO_2 (Anatase)	1	10	Two 150 W Xe lamp (λ>420 nm)	-	70% (60 min, λ>420 nm)	[13]
Pd-B	**0.02**	**10**	**24 W white LED**	**1.1 mW cm^{-2}**	**76.5% (30 min)**	**This work**

References

1 F. Rong, Q. Lu, H. Mai, D. Chen and R. A. Caruso, *ACS Appl. Mater. Interfaces*, 2021, **13**, 21138–21148.

2 I. Mukherjee, V. Cilamkoti and R. K. Dutta, *ACS Appl. Nano Mater.*, 2021, **4**, 7686–7697.

3 S. P. Tripathy, S. Subudhi, A. Ray, P. Behera, A. Bhaumik and K. Parida, *Langmuir*, 2022, **38**, 1766–1780.

4 J. Ni, J. Xue, L. Xie, J. Shen, G. He and H. Chen, *Phys. Chem. Chem. Phys.*, 2018, **20**, 414–421.

5 C. Liang, C.-G. Niu, M.-C. Shen, S.-F. Yang and G.-M. Zeng, *New J. Chem.*, 2018, **42**, 3270–3281.

6 L. Acharya, B. P. Mishra, S. P. Pattnaik, R. Acharya and K. Parida, *New J. Chem.*, 2022, **46**, 3493–3503.

7 F. Wang, Z. Zhu and J. Guo, *RSC Adv.*, 2021, **11**, 35663–35672.

8 J. Wang, L. Svoboda, Z. Němečková, M. Sgarzi, J. Henych, N. Licciardello and G. Cuniberti, *RSC Adv.*, 2021, **11**, 13980–13991.

9 R. Ji, Z. Zhu, W. Ma, X. Tang, Y. Liu and P. Huo, *Catal. Sci. Technol.*, 2020, **10**, 788–800.

10 V. Balakumar, R. Manivannan, C. Chuaicham, S. Karthikeyan and K. Sasaki, *Chem. Commun.*, 2021, **57**, 6772–6775.

11 H. Qin, Y. Yang, W. Shi and Y. She, *RSC Adv.*, 2021, **11**, 13731–13738.

12 T. Paul, P. L. Miller and T. J. Strathmann, *Environ. Sci. Technol.*, 2007, **41**, 4720–4727.

13 X. Liu, P. Lv, G. Yao, C. Ma, Y. Tang, Y. Wu, P. Huo, J. Pan, W. Shi and Y. Yan, *Colloids Surfaces A Physicochem. Eng. Asp.*, 2014, **441**, 420–426.